High Resolution Laser Spectroscopy of Dysprosium

Masterarbeit
vorgelegt von
Matthias Schmitt

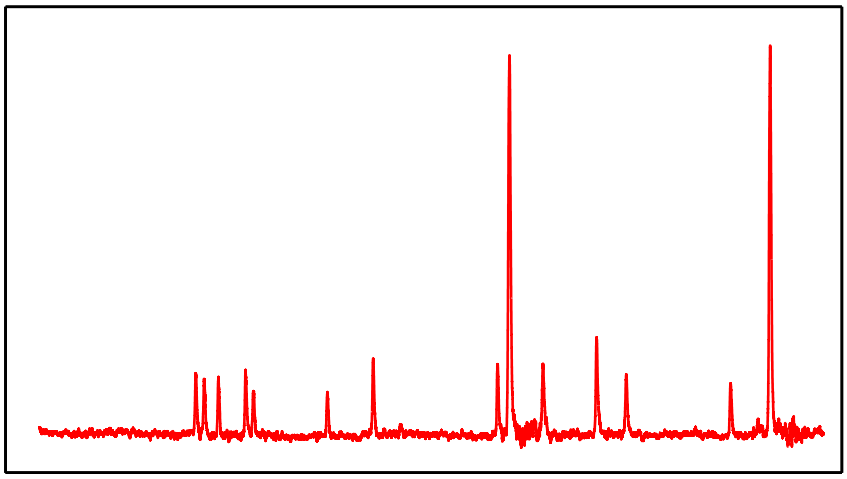

Hauptberichter: Prof. Dr. Tilman Pfau
Mitberichter: Prof. Dr. Jörg Wrachtrup

5. Physikalisches Institut
Universität Stuttgart

23. Oktober 2012

Erklärung:

Hiermit erkläre ich, dass

- ich diese Arbeit selbständig verfasst habe,
- ich keine anderen als die angegebenen Quellen und Hilfsmittel benutzt habe,
- ich alle wörtlich oder sinngemäß aus anderen Werken übernommene Aussagen als solche gekennzeichnet habe,
- die eingereichte Arbeit weder vollständig noch in wesentlichen Teilen Gegenstand eines anderen Prüfungsverfahrens gewesen ist,
- die Arbeit weder vollständig noch in Teilen bereits veröffentlicht wurde,
- der Inhalt des elektronischen Exemplars mit dem des Druckexemplars (nach § 23(7) PO) übereinstimmt.

Stuttgart, den 23. Oktober 2012

_____

(Matthias Schmitt)

Abstract

In this thesis we study two different optical transitions in the chemical element dysprosium. The measurements were done with a laser spectroscopy setup on an atomic beam in a high-vacuum chamber. We observed and characterized the hyperfine splitting of the involved excited states and the natural linewidth of the two transitions.

Contents

1. Introduction

Motivation

Since the observation of Bose-Einstein condensates (BECs) in 1995 [1–3], the dominant inter-atomic interaction that defines most of their static and dynamic properties is the isotropic short-range contact interaction. This contact interaction can be tuned using magnetic Feshbach resonances [4]. However, the research in the field of ultracold atomic gases evolved. With the first experimental realization of chromium Bose-Einstein condensates (BECs) [5] the doors to study strong inter-atomic dipole-dipole interactions in a degenerate quantum gas have been opened. In contrast with the contact interaction, the dipolar interaction is both anisotropic and long-range. These properties have attracted a lot of attention both from theoretical and experimental sides [6, 7].
Strong dipolar effects have been observed for chromium BECs: using Feshbach resonances it was shown that the contact interaction can be tuned such that it becomes negligible compared to the dipole-dipole interaction. It was shown that the expansion dynamics of the gas is strongly modified due to the presence of the strong dipolar interaction [8]. In addition, it was shown that the stability of a dipolar BEC has a strong dependence on the trap geometry [9, 10]. In contrast to the collapse of regular contact interacting BECs [11] the collapse of a dipolar BEC shows, for certain trap geometries, a d-wave shape [12]. Additionally, the dipole-dipole collisions lead to dipolar relaxations [13], which can be made useful in an almost lossless cooling mechanism, the demagnetization cooling [14].
However, within the last year, the quantum degeneracy of two different magnetic atoms was achieved: an erbium BEC [15] and a dysprosium quantum degenerate gas with both bosons [16] and fermions [17]. Both elements belong to the chemical group of the lanthanides and show a high magnetic moment ($\mu_{\mathrm{Er}} = 7\mu_{\mathrm{B}}$, $\mu_{\mathrm{Dy}} = 10\mu_{\mathrm{B}}$). As the dipolar interaction scales with the square of the magnetic moment, the dipolar effects of the two lanthanides are expected to be much stronger than in the chromium case, with $\mu_{\mathrm{Cr}} = 6\mu_{\mathrm{B}}$. Both the d-wave-like collapse and the observation of Feshbach resonances were already shown in the case of erbium. In the case of dysprosium, the dipolar interaction strength is assumed to be sufficiently strong, such that no Feshbach resonance is needed to observe strong dipolar effects. This avoids the observed atom losses near a Feshbach resonance [4]. But dysprosium does not only offer the possibility to work on dipolar effects but also gives the opportunity to search for a variation of the fine-structure constant [18], which is a highly active topic in high-precision physics [19].
At the time when the dysprosium BEC was created, we decided to change our experimental setup due to some technical limitations. As dysprosium offers the highest magnetic

moment of all atoms, we decided to continue our research on dipolar gases with dysprosium.
The first step towards the creation of an atomic quantum degenerate gas is to cool a hot atomic beam coming from an effusion oven and trap the atoms in a magneto-optical trap (MOT). A possible cooling transition for Dy is the transition at a wavelength of 421 nm. This transition being the strongest cooling transition, it is a fundamental transition for the research on ultracold dysprosium atoms. It has a natural linewidth of $\gamma_0 = 32.2\,\mathrm{MHz}$ [20], which limits the temperature of the atoms to the Doppler-temperature $T_\mathrm{D} \approx 1\,\mathrm{mK}$. To cool the atoms even further, one can use a transition with a narrower linewidth. Dysprosium offers two of those transitions, at 626 nm and at 741 nm, which have natural linewidths of $\gamma_0 = 135\,\mathrm{kHz}$ and $\gamma_0 = 1.78\,\mathrm{kHz}$ respectively. The 741 nm transition has already been used successfully to cool atoms in a MOT down to a temperature of $T = 12\mu\mathrm{K}$ [16]. To control the internal degrees of freedom of an atomic state, e.g. the creation of a fully polarized sample, one has to pump the atoms to a specific Zeeman-substate [21]. This can be done by using an optical pumping transition. Such a transition needs to be a $J \to J$ transition and in dysprosium we find this transition at a wavelength of 684 nm, where so far only the specific mass shift has been measured [22].
Both the 421 nm cooling transition and the 684 nm optical pumping transition are two important transitions on the way to create a quantum degenerate atomic gas of dysprosium, which is why we investigated them during the time of this master thesis.

About this thesis

In chapter 2 we give an overview of the properties of dysprosium. This includes the chemical properties, such as the vapor pressure and the natural abundance, and the atomic properties with the level scheme and ground and excited state properties.

In the following chapter we describe the theoretical background necessary to understand the results of this thesis. We start with the derivation of the hyperfine structure, using a multipole expansion. We continue with the natural linewidth of an energy state and describe possible broadening effects.

Chapter 4 concentrates on the methods to apply laser spectroscopy on a sample of atoms. We divide this chapter into single beam experiments, such as fluorescence and absorption spectroscopy, and Doppler-free experiments, such as saturation and polarization spectroscopy, and discuss the advantages of the different methods.

In chapter 5 we describe the experimental setup that was used for the spectroscopy measurements. We start with the laser systems that were used for the creation of the 421 nm and the 684 nm light. We continue by describing our method to calibrate the frequency during a scan of those lasers and finally describe the setup that was used to create an accessible atomic beam.

The chapters 6 and 7 finally describe the results that were obtained on the spectra of the two transitions that we considered. While the results on the 421 nm transition match those that were already known from ref. [20, 23], we investigate several spectroscopic details of the 684 nm transition, which were so far not reported in literature.

We close the thesis with a general conclusion and give an outlook on future projects.

2. Dysprosium

In this chapter we describe the element dysprosium in more details starting with chemical properties and ending with optical transitions. Dysprosium (Dy) is a rare earth element with the atomic number 66. It is a non-noble metal and therefore oxidizes at air even at room temperature. Dy has a bright silver colour and is a soft metal, which makes it machinable: it can even be cut with a knife. The melting point of Dy is at $T_{\mathrm{melt}} = 1412\,^{\circ}\mathrm{C}$ [24]. An interesting parameter for our experiment is the vapor pressure and for solid Dy this can be seen in figure 2.1. In a vacuum chamber with background pressure $p_{\mathrm{vac}} = 1 \cdot 10^{-9}$ mbar the atom flux of Dy can be detected via fluorescence light, using the strongest optical transition, starting at an oven temperature of around $T_{\mathrm{start}} = 700\,^{\circ}\mathrm{C}$. We usually work at a temperature $T_{\mathrm{work}} = 1250\,^{\circ}\mathrm{C}$.

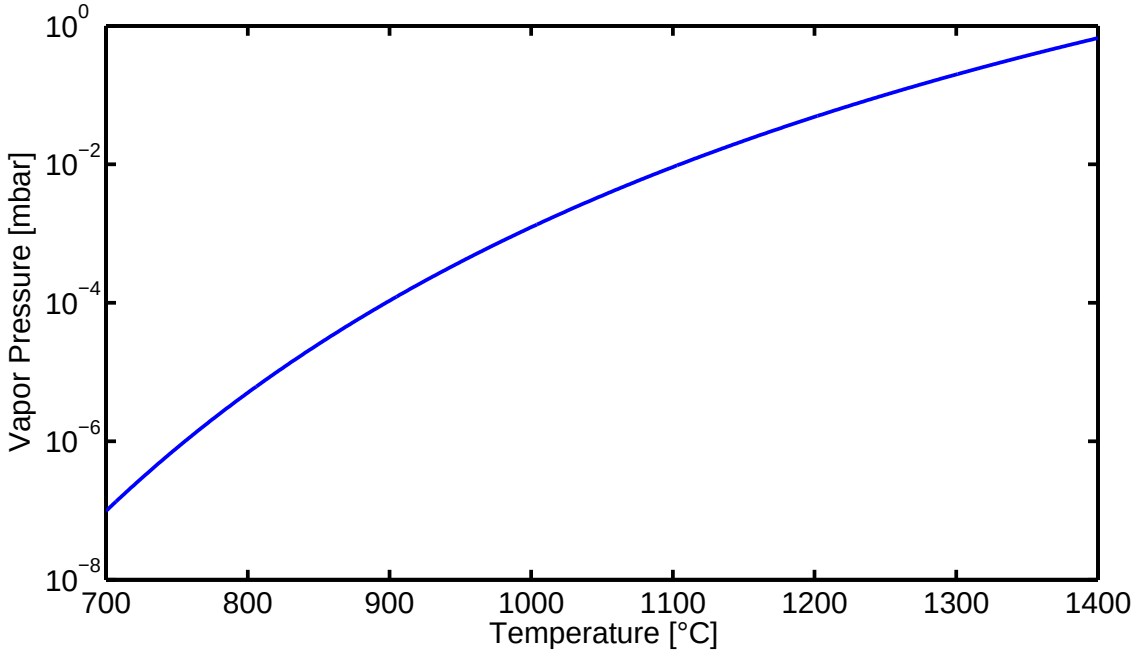

Figure 2.1.: Vapor pressure of solid dysprosium as a function of temperature.

Dysprosium has five stable isotopes, three bosonic and two fermionic, with a high natural abundance (see table 2.1) and therefore offers the opportunity to work with bosonic and fermionic isotopes. The two stable fermions have a nuclear spin of $I = \frac{5}{2}$ and therefore exhibit a hyperfine splitting of the ground state shown in figure 2.2.

isotope	mass[au]	natural abundance[%]	statistic
^{160}Dy	159.93	2.34	boson
^{161}Dy	160.93	18.91	fermion
^{162}Dy	161.93	25.51	boson
^{163}Dy	162.93	24.90	fermion
^{164}Dy	163.93	28.18	boson

Table 2.1.: Natural abundance and statistic properties of stable dysprosium isotopes [25].

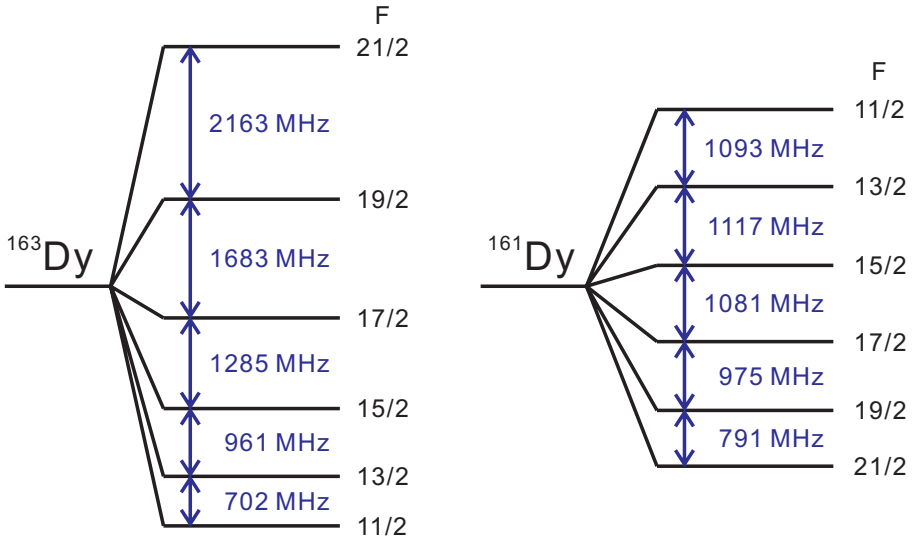

Figure 2.2.: Hyperfine splitting of the ground state of the ^{163}Dy and ^{161}Dy fermionic isotopes from ref [26].

For this thesis one has to investigate the complicated level scheme of dysprosium, partly shown in figure 2.3. Dysprosium has a $4f^{10}6s^2\,{}^5I_8$ ground state with even parity. Two optical transitions will be studied in this thesis: the 421 nm cooling transition and the 684 nm optical pumping transition:
- The cooling transition corresponds to a $4f^{10}(^5I_8)6s6p(^1P_1^0)(8,1)_9^0$ excited state with odd parity: one 6s electron is excited to a 6p electron state. The linewidth was measured to be $\gamma_{421} = 32.2\,\text{MHz}$ so we can calculate the lifetime of the excited state to $\tau_{421} = \frac{1}{2\pi\cdot\gamma_{421}} = 4.94\,\text{ns}$ [20]. The exact transition wavelength was measured to be 421.291 nm in vacuum.
- The optical pumping transition corresponds to a $4f^9(^6H^0)5d6s^2\,{}^5I_8$ excited state with an odd parity: here one of the 4f electrons is excited to a 5d electron state. So far the linewidth was only roughly estimated to $\gamma_{684} = 50 - 350\,\text{kHz}$[1]. In this thesis we measure

[1]The estimation comes from an extrapolation of relative intensities of different transitions in Dy out of the NIST atomic spectra database. The calculation itself can be found in the appendix A.2.

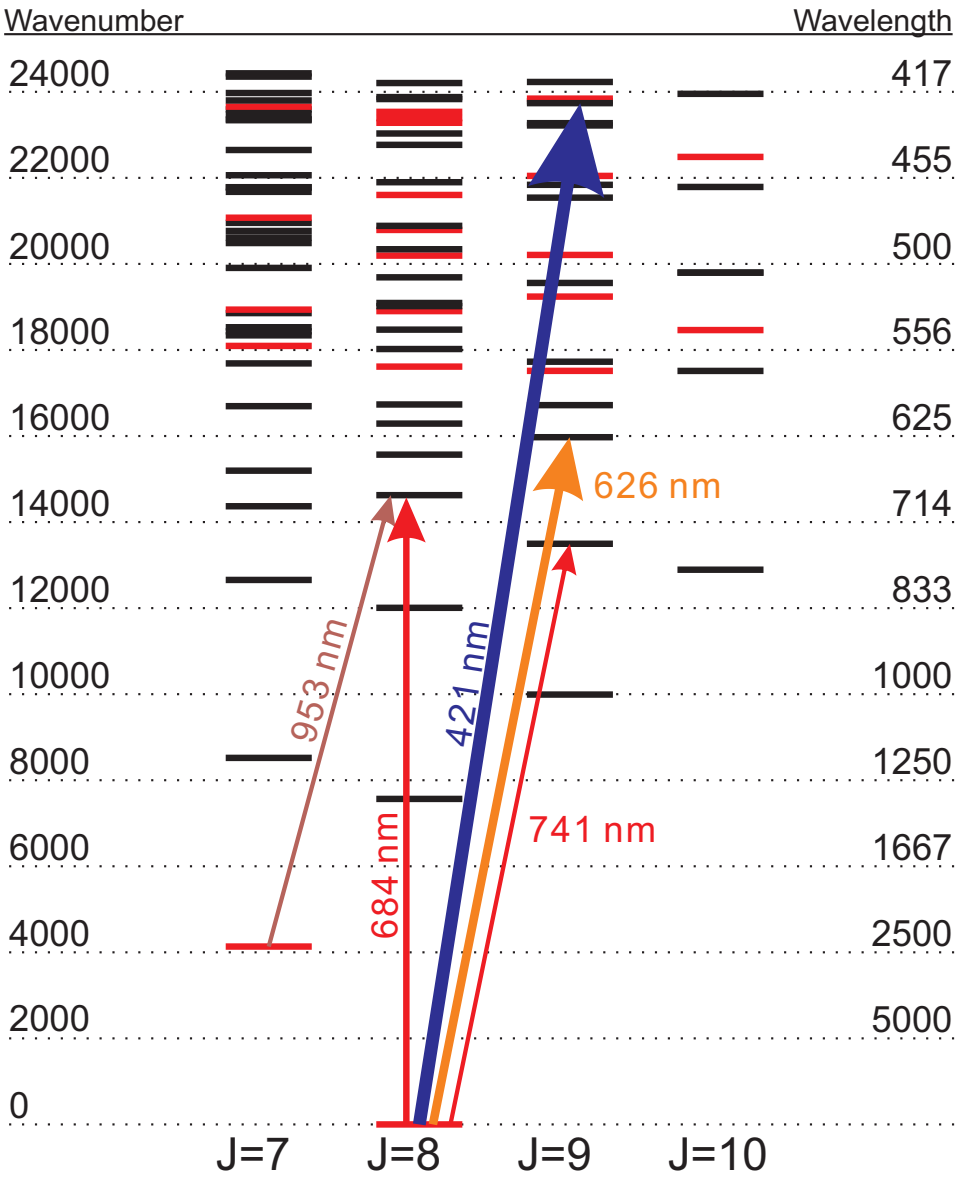

Figure 2.3.: Part of the level scheme of dysprosium [27]. Energy levels marked in red have an even parity, while levels marked in black have an odd parity. Five transitions are indicated with arrows whose thickness represents how broad is the linewidth of the corresponding transition.

the excited state lifetime and thereby calculate the linewidth of this transition (see section 7.3), providing a more accurate value.
Neither transition is closed, which means the atom can decay to some other state than the ground state. While for the cooling transition the atom can decay in many different states, for the optical pumping transition there is only one decay channel to the $4f^{10}6s^2\,{}^5I_7$

state. If needed, one could use a repumper laser at a wavelength of about 953 nm to pump the atoms back to the transition cycle. Up to now this 953 nm transition was not observed in any spectroscopical data, which could represent the strength of this decay channel to be very small.
In addition to those wavelengths there are two other laser cooling transitions in Dy, those at 741 nm and at 626 nm. Both transitions are closed transitions and can be used for narrow-line cooling and magneto-optical traps. The 741 nm transition was already successfully used, shown in ref. [16], to obtain a BEC and a Fermi-gas. We will not address such transitions further in this thesis.

3. Atomic Levels

In the following two chapters we will describe the theoretical elements necessary to understand the results obtained in this thesis. In this first chapter we will concentrate on the atomic energy levels.
From the theory of quantum mechanics we know that atoms have a quantized energy spectrum. The wavefunction of the atomic electrons is described by a few quantum numbers: the main principle quantum number N, the angular momentum quantum number L and the magnetic quantum number M. The electron carries a spin S and this spin can couple to the angular momentum via magnetic interaction, leading to a set of total angular momenta for the electron $J = |L-S|, |L-S+1|, ..., |L+S|$. This effect is called the LS-coupling, which is responsible for the fine structure and can only be obtained if we add first order relativistic corrections to the theory (see [28]).
The first section describes another structure effect, called the hyperfine structure [29], coming from the interaction of the nuclear spin with the total angular momentum of the electron. This interaction is called the IJ-coupling and is described similar to the LS-coupling. We will continue with the natural linewidth of an atomic state including broadening effects [28].

3.1. Hyperfine Structure

If we assume that the nucleus is not a massive point charge but has an inner structure, we see that the nucleus can also carry a spin I. Due to this nuclear spin, the interaction between the magnetic moment of the nucleus and the electro-magnetic field produced by the electrons leads to a new set of total angular momenta $F = |J-I|, |J-I+1|, ..., |J+I|$ (for $J > I$, similar to the LS-coupling). This new total angular momentum leads to a $(2F+1)$-fold degeneracy in the energy spectrum and the energy splitting will be derived in the following.
The Hamiltonian $\mathscr{H}$ of an atomic system can be divided in two parts if we assume that the states are perfectly isolated and can therefore be written as

$$\mathscr{H} = \mathscr{H}_{\mathrm{FS}} + \mathscr{H}_{\mathrm{HFS}}\,, \tag{3.1}$$

where the first term describes the fine structure and the second term the hyperfine structure. Furthermore, we make use of a multipole expansion for the hyperfine structure Hamiltonian. Due to symmetry arguments in parity and time-reversal, the only non-vanishing multipole terms are (apart from the electric charge) the magnetic dipole interaction, the electric quadrupole interaction, the magnetic octopole interaction, etc. For

further discussions we will only consider the first two terms, as the contribution of the higher terms is very small. The Hamiltonian for the hyperfine structure is then described by

$$\mathscr{H}_{\mathrm{HFS}} = \mathscr{H}_{\mathrm{magn.dip.}} + \mathscr{H}_{\mathrm{el.quad.}} \,. \tag{3.2}$$

We first concentrate on the magnetic dipole interaction term. We consider a point-like nuclear magnetic moment $\boldsymbol{\mu}_{\mathrm{I}}$ interacting with the magnetic field created by the electrons $\boldsymbol{B}_{\mathrm{el}}$ leading to the magnetic dipole interaction Hamiltonian

$$\mathscr{H}_{\mathrm{magn.dip.}} = -\boldsymbol{\mu}_{\mathrm{I}} \cdot \boldsymbol{B}_{\mathrm{el}} \,. \tag{3.3}$$

Here we assume that the magnetic moment can be calculated independently from the magnetic field. In addition we assume that we are working with an isolated level J (IJ-coupling approximation) so that we can write

$$\boldsymbol{B}_{\mathrm{el}} \propto \boldsymbol{J} \,. \tag{3.4}$$

Furthermore, it follows from the assumptions that

$$\boldsymbol{\mu}_{\mathrm{I}} = g_{\mathrm{I}} \mu_{\mathrm{N}} \boldsymbol{I} \propto \boldsymbol{I} \,, \tag{3.5}$$

with g_{I} the nuclear g-factor and μ_{N} the nuclear magneton. If we plug equation (3.4) and (3.5) in (3.3) we finally get

$$\mathscr{H}_{\mathrm{magn.dip.}} = A' \boldsymbol{I} \cdot \boldsymbol{J} \,. \tag{3.6}$$

By calculating the expectation value of this Hamiltonian in a basis where the matrix elements are diagonal in $\boldsymbol{I}$ and $\boldsymbol{J}$ we can calculate the energy splitting coming from the magnetic dipole interaction as

$$\Delta E_{\mathrm{magn.dip.}} = \langle \mathscr{H}_{\mathrm{magn.dip.}} \rangle = \frac{A}{2}(F(F+1) - I(I+1) - J(J+1)) \,, \tag{3.7}$$

where A has to be determined experimentally.

We now concentrate on the electronic quadrupole term. Its complete calculation can be found in [29] and we will only give an overview of it here. The general Hamiltonian for the electrostatic interaction is given by

$$\mathscr{H}_{\mathrm{el.stat.}} = \frac{-e^2}{4\pi\epsilon_0 |\boldsymbol{r}_{\mathrm{e}} - \boldsymbol{r}_{\mathrm{n}}|} \,, \tag{3.8}$$

where $\boldsymbol{r}_{\mathrm{e}}$ and $\boldsymbol{r}_{\mathrm{n}}$ are the electronic and nuclear coordinates respectively. For solving this Hamiltonian one has to separate the nuclear coordinates from the electronic ones. This allows to expand the electrostatic Hamiltonian in powers of $\frac{r_{\mathrm{n}}}{r_{\mathrm{e}}}$ as $r_{\mathrm{n}} < r_{\mathrm{e}}$. From

this expansion, one deduces the quadrupole term, which can be written as a product of spherical harmonics:

$$\begin{aligned}\mathscr{H}_{\text{el.quad.}} &= \sum_q (-1)^q Q_2^{-q}(\text{nucl.}) \cdot F_2^q(\text{el.}) \\ &= \sum_{q=-2}^{2} (-1)^q \left\{ \left(\frac{4\pi}{5}\right)^{\frac{1}{2}} e r_{\text{n}}^2 \cdot Y_2^{-q}\left(\frac{\boldsymbol{r}_{\text{n}}}{|\boldsymbol{r}_{\text{n}}|}\right) \right\} \left\{ \left(\frac{4\pi}{5}\right)^{\frac{1}{2}} \left(\frac{-e}{4\pi\epsilon_0 r_{\text{e}}^3}\right) \cdot Y_2^q\left(\frac{\boldsymbol{r}_{\text{e}}}{|\boldsymbol{r}_{\text{e}}|}\right) \right\}. \end{aligned} \tag{3.9}$$

As the spherical harmonics Y_k^q are well known we can calculate the expectation values of the two terms of equation (3.9) independently. If we do the calculation, we end up with the Hamiltonian

$$\mathscr{H}_{\text{el.quad.}} = B' \frac{3(\boldsymbol{I}\cdot\boldsymbol{J})^2 + \frac{3}{2}\boldsymbol{I}\cdot\boldsymbol{J} - I(I+1)J(J+1)}{2I(2I-1)J(2J-1)}\,. \tag{3.10}$$

Similarly to the magnetic dipole interaction we can calculate the energy splitting due to the electric quadrupole interaction

$$\Delta E_{\text{el.quad.}} = \langle \mathscr{H}_{\text{el.quad.}} \rangle = B \frac{\frac{3}{2}K(2K+1) - I(I+1)J(J+1)}{2I(2I-1)J(2J-1)}\,, \tag{3.11}$$

where B has to be determined experimentally and

$$K = \frac{1}{2}(F(F+1) - J(J+1) - I(I+1)) \tag{3.12}$$

Adding up the terms (3.7) and (3.11), which contribute to the HFS, we can calculate the total hyperfine shift

$$\Delta E_{\text{HFS}} = \Delta E_{\text{magn.dip.}} + \Delta E_{\text{el.quad.}} = AK + B \frac{\frac{3}{2}K(2K+1) - I(I+1)J(J+1)}{2I(2I-1)J(2J-1)}\,. \tag{3.13}$$

3.2. Natural Linewidth

Up to now we considered that energy states are infinitely sharp. However, experimentally, we see that if we excite an atom from the groundstate to an excited state, the atom will eventually decay back emitting a photon. If we consider having a sample of many atoms this decay probability will lead to an intensity profile. This profile of the fluorescence light[1] is represented by an exponential decay with a characteristic decay time τ given by the excited state lifetime

$$I(t) = I_0 e^{-\frac{t}{\tau}}\,. \tag{3.14}$$

[1] see section 4.1.2 for more information about the fluorescence spectroscopy

Due to Heisenberg's uncertainty relation this lifetime leads to a minimal width of the state in the energy spectrum: $\Delta E \geq \hbar/\Delta t$. We can express the energy as $E = \hbar\omega = \hbar(2\pi\nu)$ leading to the natural linewidth γ_0 for the excited state

$$\gamma_0 \equiv \Delta\nu = \frac{1}{2\pi\tau}\,. \tag{3.15}$$

To investigate the spectral distribution of the fluorescence light we describe the excited electron classically using the model of a damped harmonic oscillator [30]. Its oscillations are described by the differential equation of motion:

$$\ddot{x} + \gamma\dot{x} + \omega_0^2 x = 0\,, \tag{3.16}$$

with the damping constant γ and the resonance frequency $\omega_0 = \sqrt{\frac{k}{m_\mathrm{e}}}$ with the restoring force constant k and the electron mass m_e. If we consider that the damping is small compared to the oscillation frequency ($\gamma \ll \omega_0$) the real part solution writes

$$x(t) = x_0 e^{-\frac{\gamma}{2}t}\cos(\omega_0 t)\,. \tag{3.17}$$

We can finally obtain the frequency distribution via Fourier transformation

$$A(\omega) = \frac{1}{\sqrt{2\pi}}\int_{-\infty}^{+\infty} x(t)e^{-i\omega t}\,\mathrm{d}t = \frac{1}{\sqrt{2\pi}}\int_{0}^{+\infty} x_0 e^{-\frac{\gamma}{2}t}\cos(\omega_0 t)e^{-i\omega t}\,\mathrm{d}t\,, \tag{3.18}$$

with $x(t<0) = 0$. The integration of equation (3.18) gives the complex amplitude $A(\omega)$, which splits into a rotating/resonant term and a counter rotating/antiresonant term

$$A(\omega) = \frac{x_0}{\sqrt{8\pi}}\left(\frac{1}{i(\omega-\omega_0)+\frac{\gamma}{2}} + \frac{1}{i(\omega+\omega_0)+\frac{\gamma}{2}}\right)\,. \tag{3.19}$$

The real intensity is obtained by multiplying equation (3.19) with its complex conjugate. For an atomic transition follows $\omega_0 \gg |\omega - \omega_0|$ and we can therefore make use of the rotating wave approximation and neglect the antiresonant $(\omega + \omega_0)$ terms. This leads to the following intensity profile

$$I(\omega-\omega_0) = \frac{I_0\gamma}{2\pi((\omega-\omega_0)^2 + (\frac{\gamma}{2})^2)}\,. \tag{3.20}$$

It describes a Lorentzian profile with a full width at half-maximum (FWHM) equal to the linewidth and a peak intensity $I(\omega_0) = \frac{2I_0}{\pi\gamma}$.

3.3. Linewidth Broadening Effects

In addition to the natural linewidth of an optical transition there exist broadening mechanisms. Those important for our measurements, as they have a strong influence on the measured linewidth, are the Doppler broadening, the pressure broadening and the power broadening. They are discussed in the following.

3.3.1. Doppler broadening

Due to the Doppler effect, the emitted frequency of an atom changes depending on the relative movement between the atom and the observer according to

$$\omega = \omega_0 + \boldsymbol{k} \cdot \boldsymbol{v}\,, \tag{3.21}$$

with the central frequency ω_0 defined as the frequency with no relative movement, the wave vector $\boldsymbol{k}$ and the velocity of the atom $\boldsymbol{v}$. We choose the z-direction as the direction of the laser beam used for the excitation of the atom and rewrite equation (3.21) as

$$\omega = \omega_0 + \omega_\mathrm{D} = \omega_0 \left(1 + \frac{v_\mathrm{z}}{c}\right)\,, \tag{3.22}$$

with ω_D defined as the Doppler-shift. At thermal equilibrium at temperature T, the number of atoms $(n_\mathrm{i}(v_\mathrm{z})\mathrm{d}v_\mathrm{z})$ within the velocity interval dv_z follow a Maxwellian velocity distribution:

$$n_\mathrm{i}(v_\mathrm{z})\mathrm{d}v_\mathrm{z} = \frac{N_\mathrm{i}}{v_\mathrm{p}\sqrt{\pi}} e^{-(\frac{v_\mathrm{z}}{v_\mathrm{p}})^2} \mathrm{d}v_\mathrm{z}\,, \tag{3.23}$$

with N_i describing the total number of atoms. Here $v_\mathrm{p} = \sqrt{\frac{2k_\mathrm{B}T}{m}}$ describes the most probable velocity with the atomic mass m and the Boltzmann constant k_B. As the velocity is connected to the frequency by equation (3.22) we can modify equation (3.23). The Doppler-broadened intensity profile then writes

$$I(\omega) = I_0 exp\left[-\left(\frac{c(\omega-\omega_0)}{\omega_0 v_\mathrm{p}}\right)^2\right]\,. \tag{3.24}$$

If we consider the finite lifetime of the atomic energy levels, it becomes clear that the Doppler-broadening is not only described by a Gaussian profile but is given by the convolution of the Doppler-broadened profile with the Lorentzian frequency distribution of the atomic level. With this, the intensity profile becomes

$$I(\omega) = C \int_0^{+\infty} \frac{\exp\left[-\left(\frac{c(\omega-\omega_0)}{\omega_0 v_\mathrm{p}}\right)^2\right]}{(\omega-\omega')^2 + \left(\frac{\gamma}{2}\right)^2} \mathrm{d}\omega'\,, \tag{3.25}$$

with $C = \frac{\gamma N_\mathrm{i} c}{2v_\mathrm{p}\sqrt{\pi^3}\omega_0}$. This kind of profile is called a Voigt profile. It describes, on the one hand, the natural linewidth γ of the energy state and, on the other hand, the width of the Maxwellian velocity distribution $\delta\omega_\mathrm{D} = 2\sqrt{\ln 2}\omega_0 \frac{v_\mathrm{p}}{c}$, called the Doppler width.

3.3.2. Power broadening

Another broadening effect is known as power or saturation broadening. It is due to laser intensities higher than the saturation intensity of the transition. To understand this

effect we have to look at the rate equation in a two-level system. The rate equation for the population of each level depends on the absorption probability P_{ij} for a transition $|i\rangle$ to $|j\rangle$ and the relaxation probability R_{i} for a level $|i\rangle$ and is given by

$$\frac{\mathrm{d}N_1}{\mathrm{d}t} = -\frac{\mathrm{d}N_2}{\mathrm{d}t} = -P_{12}N_1 - R_1N_1 + P_{12}N_2 + R_2N_2\,. \tag{3.26}$$

With $N = N_1 + N_2$ and $P = P_{12} = P_{21}$, the population densities can be written as

$$N_{1,2} = N\frac{P + R_{2,1}}{2P + R_1 + R_2}\,. \tag{3.27}$$

Let us consider the two extreme cases:
- For $P \to \infty$ we end up with $N_1 = N_2 = \frac{N}{2}$.
- For $P = 0$ the population of the two levels become

$$N_{10,20} = \frac{R_{2,1}}{R_1 + R_2}\,. \tag{3.28}$$

In between those extreme cases, the difference between the populations of the two levels is given by

$$\Delta N = N_1 - N_2 = \frac{\Delta N_0}{1 + \frac{2P}{R_1+R_2}} = \frac{\Delta N_0}{1+S}\,. \tag{3.29}$$

with $\Delta N_0 = N_{10} - N_{20}$ and the saturation parameter $S = \frac{2P}{R_1+R_2}$ representing the ratio of pumping rate and average relaxation.
Since the natural linewidth of an energy state has a Lorentzian profile we have to consider a frequency-dependent saturation parameter. This profile has also a Lorentzian frequency dependence [30]:

$$S(\omega) = S(\omega_0)\frac{\left(\frac{\gamma}{2}\right)^2}{(\omega-\omega_0)^2 + \left(\frac{\gamma}{2}\right)^2}\,. \tag{3.30}$$

From this we can calculate the intensity profile

$$I_{\mathrm{s}}(\omega) = I_0(\omega_0)\frac{\left(\frac{\gamma_{\mathrm{S}}}{2}\right)^2}{(\omega-\omega_0)^2 + \left(\frac{\gamma_{\mathrm{S}}}{2}\right)^2}\,, \tag{3.31}$$

and we define the saturated linewidth γ_{S} as

$$\gamma_{\mathrm{S}} = \gamma_0\sqrt{1+S_0} = \gamma_0\sqrt{1+\frac{I'}{I'_{\mathrm{S}}}}\,, \tag{3.32}$$

with the natural linewidth γ_0 and $S_0 = \frac{I'}{I'_{\mathrm{S}}}$ [31], where I'_{S} is the saturation intensity of the transition considered and I' the used laser intensity. The intensity profile has still a Lorentzian profile but with a different linewidth, e.g. if we drive a transition with a laser

power comparable to the saturation intensity, the obtained linewidth will be $\gamma = \sqrt{2}\gamma_0$. While the peak intensity $I(\omega_0)$ grows linearly with the power of the probe beam, we find a different dependence to the power of the pump beam. To explain this we have to look at the population of the excited state N_2. With the assumption of a stable groundstate N_1 we can set the relaxation probability $R_1 = 0$ and write equation (3.27) as

$$N_2 = N\frac{P}{2P + R_2}\,. \tag{3.33}$$

With the definition of the saturation parameter $S = \frac{2P}{R_1+R_2}$ and the assumption $R_1 = 0$ we can write equation (3.33) in dependence of the intensity as

$$N_2 = \frac{N}{2}\frac{S}{1+S} = \frac{N}{2}\frac{I'/I'_S}{1 + I'/I'_S}\,. \tag{3.34}$$

Here, we see again that in the extreme case of infinite pump power the population in the excited state becomes $\lim\limits_{I'\to\infty} N_2 = \frac{N}{2}$.

3.3.3. Pressure broadening

The last effect we will consider is the pressure broadening. It is due to collisions between the atoms and a background gas or between the atoms themselves. As this effect is negligible for our setup we will only give the basic ideas while the complete calculation can be found in [30]. There are two kinds of collisions: elastic and inelastic ones.
- If we excite an atom A during an elastic collision with an atom or molecule B we will observe a positive (negative) energy shift of the excited state depending if the interaction is repulsive (attractive).
- In the case of an inelastic collision the spectral line is broadened up. This comes from the fact that this kind of collision leads to an additional depopulation of the excited state besides the decay channel due to the spontaneous emission. As those collisions are depending on the pressure, the transition probability and therefore the linewidth are also pressure-dependent

$$\gamma = \gamma_0 + \gamma_{\text{press}} = \gamma_0 + a p_{\text{B}}\,, \tag{3.35}$$

with the pressure of the collision partner p_{B} and $a = 2\sigma_{\text{ik}}\sqrt{\frac{2}{\pi\mu k_{\text{B}}T}}$ with the scattering cross section σ_{ik}, the reduced mass μ and the gas temperature T.

If we take into account both types of collisions and we consider again a classical harmonic damped oscillator ansatz, we will end up with a Lorentzian intensity profile

$$I(\omega) = \frac{C}{(\omega - \omega_0 - \Delta\omega)^2 + \left(\frac{\gamma_0+\gamma_{\text{press}}}{2}\right)^2}\,, \tag{3.36}$$

where $\Delta\omega$ is proportional to the cross section σ_{s} of elastic collisions responsible for the line shift and γ_{press} is proportional to the cross section σ_{b} of inelastic collisions responsible for the line broadening.

4. Laser Spectroscopy

In this chapter, we discuss different approaches on the observation of an energy level. A well known technique is the use of laser spectroscopy where laser light is used to detect the transition from a known state, e.g. the groundstate, to the state one wants to detect. Here, we discuss tow types of methods, single-beam and Doppler-free ones. We also comment on an important electronic device for our measurements: the lock-in amplifier.

4.1. Single-Beam Methods

We first concentrate on the single-beam methods. As the name already tells, those methods are based on one laser beam shooting on a sample. As a consequence, the corresponding setup is rather simple to realize. However, the major disadvantage of this method is that it is limited by the Doppler-broadening effect described in section 3.3.1. In the following subsections we will discuss the absorption spectroscopy and the fluorescence spectroscopy as the two possible single-beam methods.

4.1.1. Absorption Spectroscopy

The setup of an absorption spectroscopy is shown in figure 4.1. A laser beam is sent through a sample of atoms with the transmitted light being measured with a photodiode. In the following we will describe an example on how the Doppler-broadening can affect the measurements in the case of a thermal cell. In our setup we use a laser beam perpendicular to an atomic beam, which is why we only have a "residual" Doppler-effect coming from the fact that atomic beam is diverging.
Let us assume that we only have a stable ground state, which means that $\tau \to \infty$, and one excited state with a natural linewidth of 10 MHz and a transition wavelength of $\lambda = 500\,\text{nm}$. If our cell has a temperature of T=100 °C and we have an atomic mass of

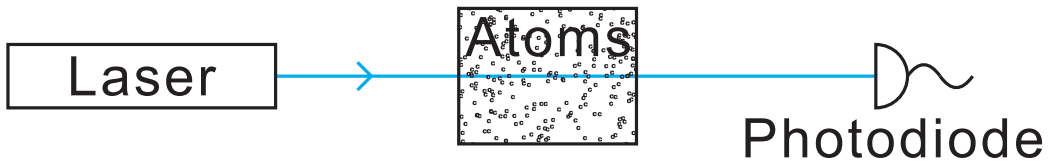

Figure 4.1.: Absorption spectroscopy method: a laser beam is send through an atomic sample and a photodiode measures the transmitted light.

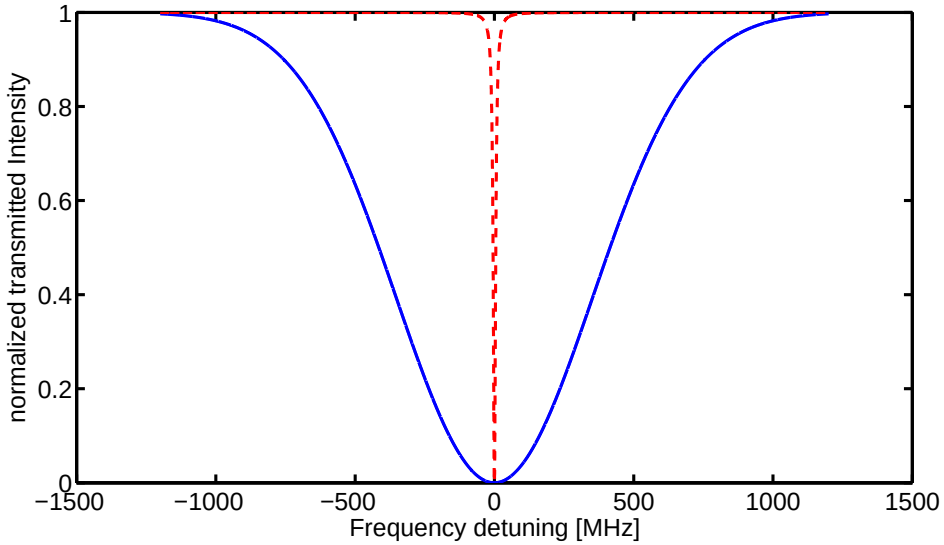

Figure 4.2.: Typical absorption signal: the normalized transmitted intensity is plotted over the region of the resonance frequency. This plot assumes that the laser intensity is lower than the saturation intensity so the light is completely absorbed at the resonance. The blue curve shows a Gaussian profile (3.24) with a width of 830 MHz while the red dashed curve describes the Lorentzian profile (3.20) with the natural linewidth of 10 MHz, which would be present in absence of Doppler broadening.

m=100 u we can calculate the most probable velocity: $v_\mathrm{p} \approx 249\,\frac{\mathrm{m}}{\mathrm{s}}$. Out of those values we can calculate that the Doppler width is around $\gamma_\mathrm{D} \approx 830\,\mathrm{MHz}$. We are working with a low pressure and a laser intensity smaller than the saturation intensity of our transition to be able to neglect pressure and intensity broadening. With this the light is completely absorbed at resonance. Furthermore, we scan the laser over the resonance and observe the transmitted light through the cell, as shown in figure 4.2. The Doppler width is much larger than the natural linewidth and therefore we can assume the Gaussian profile as a good approximation (see section 3.3.1). In this example, the Doppler-broadening dominates the absorption profile and therefore this spectroscopic method cannot be used for high resolution measurements.

4.1.2. Fluorescence Spectroscopy

The fluorescence spectroscopy uses a similar setup compared to the absorption spectroscopy, shown in figure 4.3. The only difference is the detection: here we do not detect the transmitted light of the beam, but collect the fluorescence light from the atoms. As this light is emitted across the solid angle 4π, the efficiency will not be as high as for the absorption spectroscopy as we cannot collect the whole light but only a fraction of the solid angle. Still we get a sufficiently good signal when bringing a lens as close as possible to the atoms and focus it onto a photodiode. If we now scan the laser over the resonance

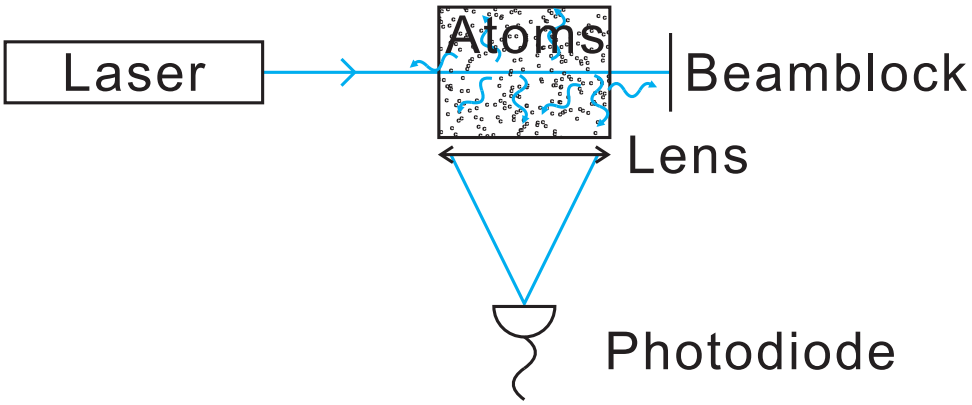

Figure 4.3.: Fluorescence spectroscopy method: a laser beam is send through a sample of atoms and we collect the fluorescence light emitted by the atoms.

we will find the signal shown in figure 4.2 but inverted.
Besides this, the fluorescence spectroscopy offers the possibility for precision lifetime measurements. For this measurement we have to lock the laser in frequency to be always resonant with the atomic transition. We then suddenly turn off the laser light and obtain a exponential decay of the fluorescence light over time. Here, the characteristic decay time corresponds to the excited state lifetime τ_e. This method can be challenging if we have a broad natural linewidth. For our example the linewidth is 10 MHz which translates to an

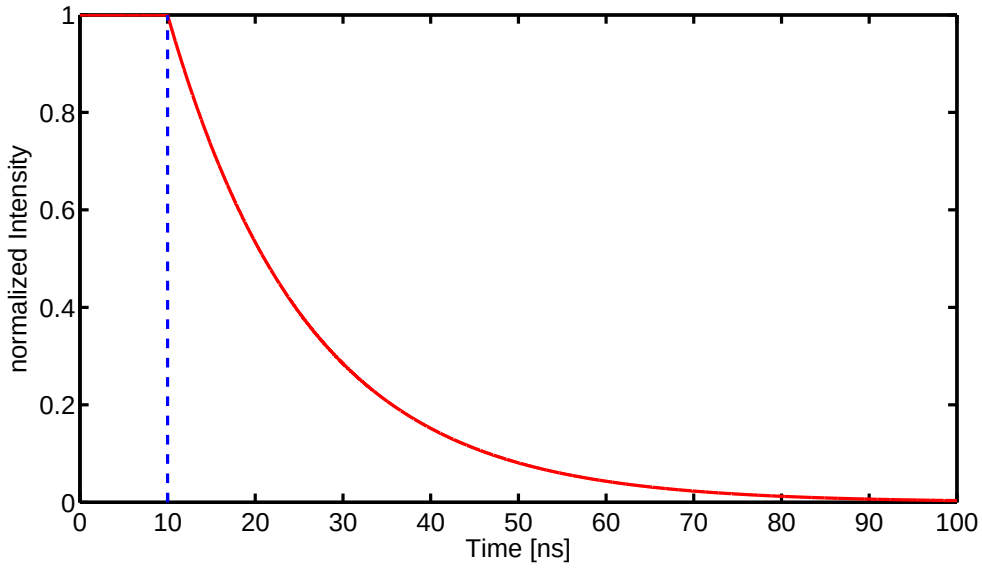

Figure 4.4.: Fluorescence decay signal: the normalized intensity is plotted over the time. The red curve shows the intensity that can be measured on a photodiode. In this plot the laser light is turned off at the position of the dashed blue line (10 ns).

excited state lifetime of $\tau_e = \frac{1}{2\pi\gamma_0} \approx 16\,\text{ns}$. This short lifetime has two important consequences: First, we have to consider the time needed to turn off the laser light completely. Second, the photodiode has to be fast enough to see this decay. If those two conditions are fulfilled, we can obtain a signal similar to the one shown in figure 4.4. In this example we assume that our laser light is instantly turned off after 10 ns.
The fluorescence spectroscopy is still limited by the Doppler-broadening but can be used for a direct measurement of the excited state lifetime to calculate the linewidth of a transition.

4.2. Doppler-Free Methods

To get rid of the Doppler-broadening effect we now make use of two laser beams propagating in counter-direction through the sample. The two important spectroscopy methods for us will be the saturated absorption spectroscopy and the polarization spectroscopy.

4.2.1. Saturated Absorption Spectroscopy

The setup for this method is shown in figure 4.5. We divide the beam into two parts using a beam splitter: a weak probe beam and a stronger pump beam. Both beams are guided in a counter-propagating way through the atomic sample while only the probe beam is detected.

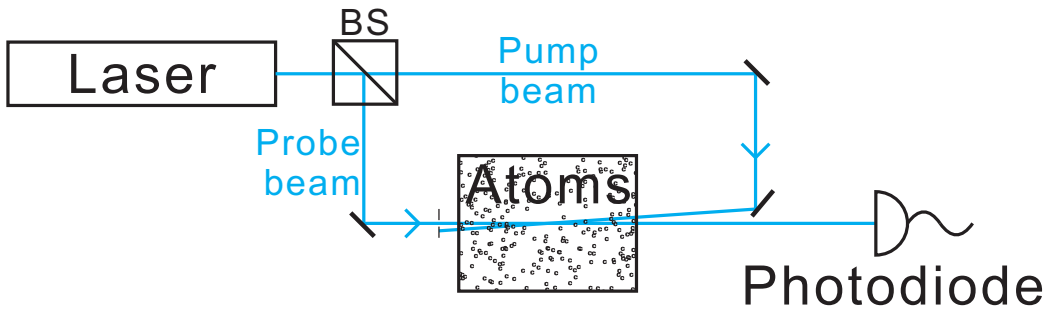

Figure 4.5.: Scheme for the saturated absorption spectroscopy method. The laser beam is split with a beamsplitter (BS) into two beams: the probe and the pump beam, which are guided in a counter-propagating way through the atomic sample. Here, only the probe beam is detected with a photodiode.

We assume again that the intensity of the probe beam is lower than the saturation intensity of the transition, and the one of the pump beam is equal to the saturation intensity. The laser frequency is scanned over the transition resonance and the intensity of the probe beam during the scan can be seen in red in figure 4.6.
The detected signal corresponds to the sum of the Doppler-broadened absorption signal (see figure 4.2) and the natural linewidth at the center of the resonance. To explain this

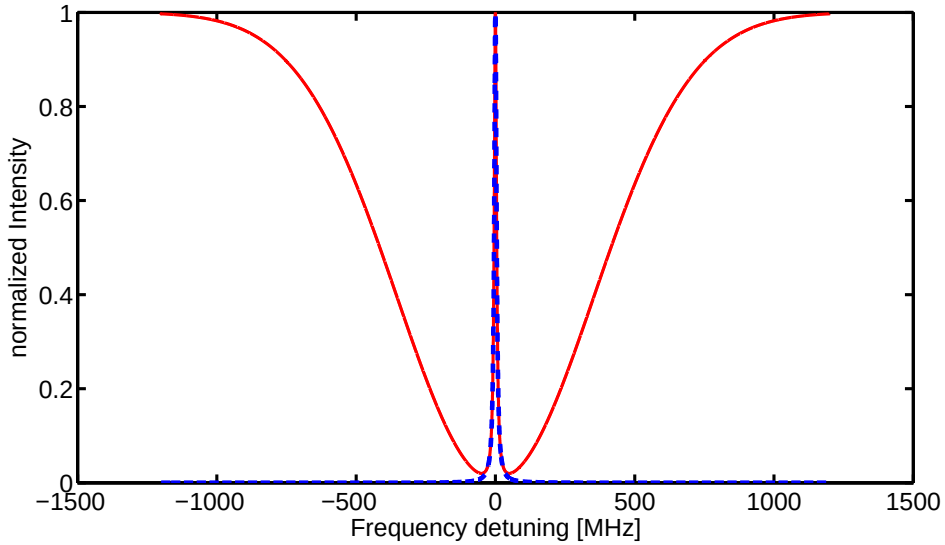

Figure 4.6.: Saturated absorption signal: The Doppler-broadened absorption signal including a narrow Lorentzian-shaped peak at the center is plotted in red. With the use of a lock-in amplifier we can get rid of the Doppler-broadened background and get the signal shown as dashed blue line.

signal we have to take a closer look to the Doppler effect again. As it can be seen from equation (3.22), $\omega = \omega_0 + \omega_D = \omega_0 \left(1 + \frac{v_z}{c}\right)$, we can associate a frequency to a velocity. If an atom (representing a velocity class of atoms) is propagating in the direction of the probe beam it can be excited if the frequency of the laser fulfills equation (3.22). As a consequence, at this frequency the pump beam is far off-resonant to the same atom and the probe beam is absorbed. We only find the same transition frequency for probe and pump beam if the atom is at rest. Both beams are now acting on the same atom. As the intensity of the pump beam is much higher than the one of the probe beam, the atom will be excited by the pump beam and therefore the probe beam will be completely transmitted, giving rise to the central feature in the signal shown in figure 4.6.

To improve the signal-to-noise ratio and to get rid of the Doppler-broadened background, a lock-in amplifier is often used. To be able to use a lock-in amplifier we need to chop the intensity of the pump beam with a rectangular modulation between zero and one at a frequency f_{chop}. In a simplified picture the lock-in amplifier is subtracting the signal without pump beam from the signal with pump beam on. In more details, within the lock-in amplifier the signal of the photodiode is multiplied with the same chopping frequency and demodulated considering the phase between the signal and the reference chopping signal. Simultaneously, as electronic noise is decreasing with the frequency, this means that the higher the chopping frequency, the lower the noise. The signal of the spectrum with lock-in amplifier can be seen in figure 4.6 as blue dashed line.
A common method to chop the intensity of a laser beam is the use of an acousto-optical

modulator (AOM) in the path of the laser beam. One important fact to be considered is that the AOM also shifts the frequency of the laser beam. As the spectroscopy method is depending on the absolute frequency of both beams we have to find the new resonance condition where both laser beams are acting on the same velocity class. We define ω_L as absolute laser frequency, ω_0 as resonance frequency of the transition, $\Delta\omega_D$ as Doppler-shift and $\Delta\omega_{1,2}$ as the frequency shift in the probe or pump beam respectively. The resonance conditions for the pump and the probe beams are given by

$$\omega_0 = \omega_L + \Delta\omega_1 + \Delta\omega_D \tag{4.1}$$

$$\omega_0 = \omega_L + \Delta\omega_2 - \Delta\omega_D\,. \tag{4.2}$$

If we take the sum of those two equations we already see that the Doppler-shift cancels out and we find the following condition

$$\omega_L = \omega_0 - \frac{\Delta\omega_1 + \Delta\omega_2}{2}\,. \tag{4.3}$$

This means that for a positive frequency shift, the laser has to have a lower frequency compared to the transition frequency to observe a resonance with the atoms.

4.2.2. Polarization Spectroscopy

The saturated absorption spectroscopy is a good method to directly measure the linewidth of a transition. However it does not allow to frequency stabilize a laser to such a transition. This can be realized using the polarization spectroscopy method, which we discuss in this section.

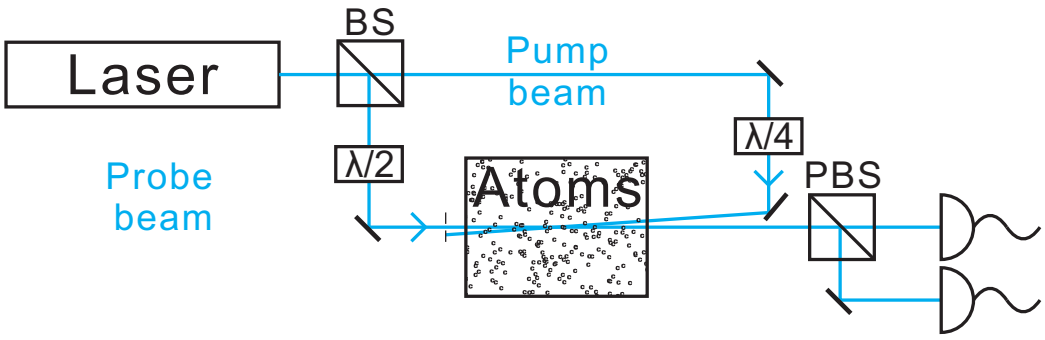

Figure 4.7.: Scheme of the polarization spectroscopy method: the laser beam is split with a beamsplitter (BS) into two beams, probe and pump, which are guided in a counter-propagating way through the atomic sample. The probe beam is guided through a $\frac{\lambda}{2}$-waveplate to align the linear polarization while the pump beam is guided through a $\frac{\lambda}{4}$-waveplate to create circular polarized light. The transmitted probe beam is split into two using a polarizing beam splitter (PBS) and detected with two photodiodes in a light-balancing setup.

The setup is very similar to the one just described in the saturated absorption spectroscopy and can be seen in figure 4.7. Here the pump beam is circularly polarized with a $\frac{\lambda}{4}$-waveplate while the linear polarization of the probe beam can be changed with a $\frac{\lambda}{2}$-waveplate. The probe beam is guided through the sample of atoms before being split with a polarization beam splitter (PBS). It is finally detected with a light balancing photodiode system with the use of a lock-in amplifier. The signal that we can observe is shown in figure 4.8. To understand the shape of the signal we have to take a look into the theory [32, 33].

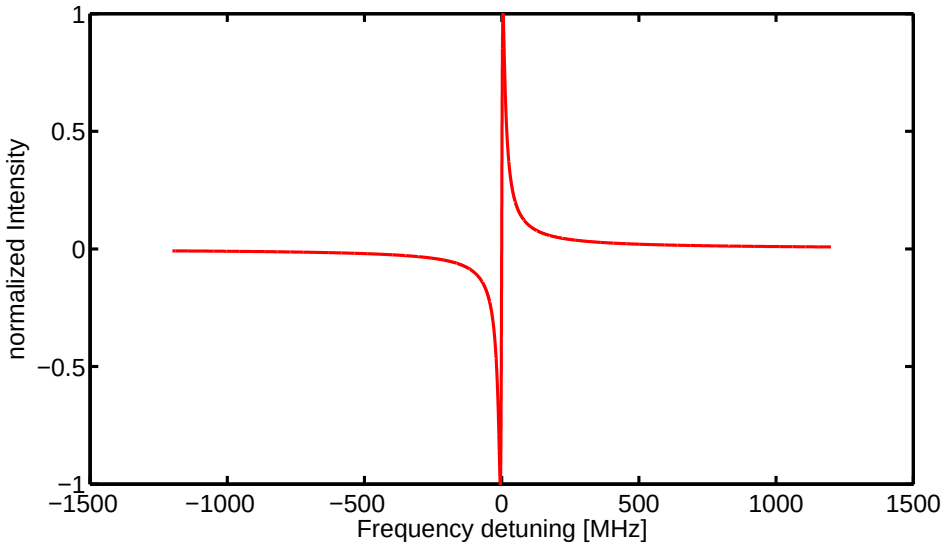

Figure 4.8.: Example for a polarization spectroscopy signal. The values were taken from the example in section 4.1.1. The steep slope can be used for the frequency lock of a laser.

A linearly polarized beam can be seen as a superposition of two circular polarized beams with equal amplitude but opposite polarization. Considering the light propagating in z-direction we can write the electric field of the beam in terms of circular polarized basis vectors as

$$\boldsymbol{E} = \begin{bmatrix} E_\mathrm{x} \\ E_\mathrm{y} \end{bmatrix} = E_0 \begin{bmatrix} \cos\phi \\ \sin\phi \end{bmatrix} = E_0 \left\{ \frac{\mathrm{e}^{-\mathrm{i}\phi}}{2} \begin{bmatrix} 1 \\ \mathrm{i} \end{bmatrix} + \frac{\mathrm{e}^{\mathrm{i}\phi}}{2} \begin{bmatrix} 1 \\ -\mathrm{i} \end{bmatrix} \right\} \tag{4.4}$$

As we have circularly polarized pump light (e.g. σ^+) the medium has different absorption coefficients and refractive indices for σ^+ and σ^- light, we define $\Delta\alpha = \alpha_+ - \alpha_-$ and $\Delta n = n_+ - n_-$ as the difference in absorption coefficient and refractive index. After a cell of length L, and assuming that the birefringence of the windows is negligible, the electric field of the transmitted probe beam writes

$$\boldsymbol{E} = E_0 \exp\left\{ -\frac{\mathrm{i}\omega n L}{c} - \frac{\alpha L}{2} \right\} \left\{ \frac{\mathrm{e}^{-\mathrm{i}\phi}}{2} \begin{bmatrix} 1 \\ \mathrm{i} \end{bmatrix} \mathrm{e}^{\mathrm{i}\Omega} + \frac{\mathrm{e}^{\mathrm{i}\phi}}{2} \begin{bmatrix} 1 \\ -\mathrm{i} \end{bmatrix} \mathrm{e}^{-\mathrm{i}\Omega} \right\}, \tag{4.5}$$

with $\Omega = \frac{\omega}{2c}\Delta n L - i\frac{L}{4}\Delta\alpha$, $\alpha = \frac{1}{2}(\alpha_+ + \alpha_-)$ and $n = \frac{1}{2}(n_+ + n_-)$. As the intensity is the square of the electric field ($I \propto |E|^2$) the measured intensity signal can be written as the difference between the intensity of the two perpendicular polarizations I_x and I_y

$$I = I_\mathrm{x} - I_\mathrm{y} = I_0 \mathrm{e}^{-\alpha L} \cos\left(2\phi + L\Delta n \frac{\omega}{c}\right) . \tag{4.6}$$

To get rid of the refractive index we use the Kramers-Kronig dispersion relation [34] to connect it to the absorption coefficient. We finally obtain the simplified signal shape if we assume that the rotation of the polarization induced by the medium is small with a maximal signal at $\phi = \frac{\pi}{4}$ and add the Lorentzian lineshape as natural linewidth (see equation (3.2)):

$$I = -I_0 \mathrm{e}^{-\alpha L} \left(L\Delta\alpha_0 \frac{x}{1+x^2}\right) , \tag{4.7}$$

with $x = \frac{2(\omega-\omega_0)}{\gamma_0}$. This signal shows a dispersive-like behavior.
In fact for frequency stabilization, we are not really interested in the signal shape but rather in the slope around the zero-crossing. The interesting part here is the frequency difference between the maximum and the minimum of the slope, which is given by the linewidth of the transition. With the slope m and the maximum peak-to-peak noise $I_\mathrm{noise,pk\text{-}pk}$ we can calculate the maximal frequency drift $\delta\nu$ of the frequency lock to

$$\delta\nu = \frac{I_\mathrm{noise,pk\text{-}pk}}{m} . \tag{4.8}$$

As this spectroscopy method is depending on the polarization of the pump and the probe beams, we expect a change in the signal depending on magnetic fields, which will align the spin of the electrons. The most efficient way is to align the quantization axis defined by the magnetic field along the propagation axis of the excitation laser. In this case we will find an increase of the signal, estimated to have a linear dependence with the strength of the magnetic field. In addition the magnetic field leads to a Zeeman-shift of the different m_J sublevels depending on the g-factors of the involved states. In our case the g-factors are almost the same, which is why we can neglect this effect.

5. Experimental Setup

In this chapter we discuss the experimental setup that we use to perform spectroscopic measurements. In section 5.1 we describe the creation of tunable laser light at the wavelengths of the transitions that we would like to analyze. The second required step is to have a source of dysprosium atoms and two different approaches have been tested within the work of this thesis. Here we will concentrate on the most promising approach based on an atomic beam, which we present in section 5.2. The second approach, based on a hollow cathode lamp, can be found in the appendix A.1

5.1. Laser System

As we want to perform laser spectroscopy on dysprosium atoms we need on the one hand to have a stable laser light source at the transition wavelengths (see chapter 2). On the other hand we need to be able to tune the wavelength of the laser light. This tuning range has to be large enough to see a complete spectrum of the transition that we want to analyze, which is on the order of a few GHz. Tuning the wavelength can be either done with electro-optical or acousto-optical devices, standing in the path of the laser beam, or with the source itself. In our case we tune the wavelength directly with the light source, as we explain in more details in the following subsections 5.1.1 and 5.1.2.

5.1.1. 421nm Cooling Transition

As described in chapter 2, a possible cooling transition for dysprosium is the transition at 421 nm. The production of this 421 nm light is not easy to achieve with a single light source, so we need to go through three steps, which can be seen in figure 5.1: We start with a light source at 532 nm[1]. This 532 nm light is used to pump a Titanium:Sapphire laser (Ti:Sa)[2]. The Ti:Sa itself emits again light at a wavelength of 842 nm with a power of 3.1 W. As a last step this 842 nm light is frequency-doubled, with a brewster-cut Lithium Triborate crystal (LBO) placed inside a monolithic ring cavity, to 421 nm light with a power of 800 mW. As this crystal is only brewster-cut for the 842 nm light there is a reflection of the 421 nm light at the edge of the crystal (see [35]). The reflected light is extracted out of the cavity and forms the beam used for the spectroscopic measurements.

[1] Coherent Verdi V18
[2] Coherent MBR110

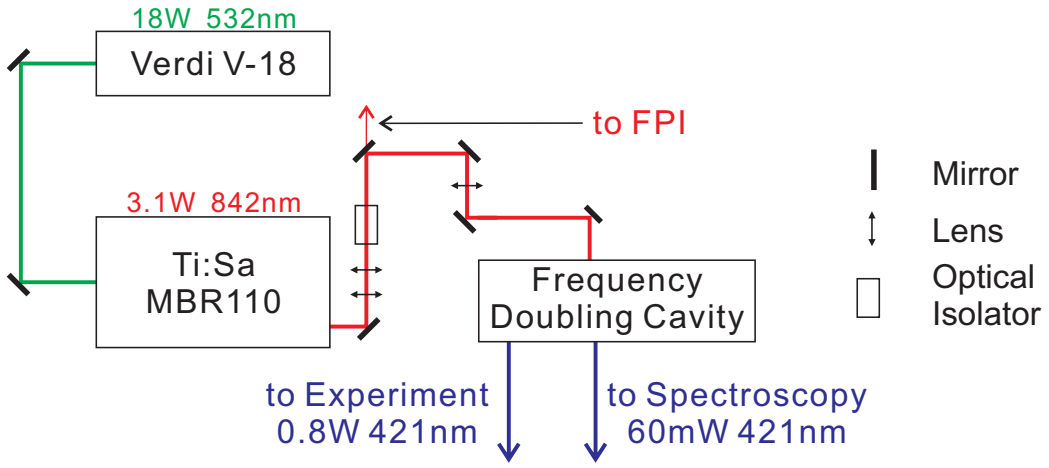

Figure 5.1.: Technical drawing of the 421 nm laser light production: 532 nm light is pumping a Ti:Sa, which emits itself at 842 nm. The 842 nm are finally frequency-doubled to 421 nm. [35]

As mentioned before we need a tunable light source. For this we use the Ti:Sa which is producing the 842 nm light. The overall tuning range of the Ti:Sa is 700 nm-1030 nm. The dynamic tuning range, where the laser is still running in single mode is up to around 40 GHz, which is sufficient for our needs. This scan can be controlled in two ways: The wavelength can either be scanned within the Ti:Sa control unit or with an external voltage ramp. Both methods were tested and for this work the internal scan of the Ti:Sa was used to perform the measurements as this method assures that the laser stays locked during the scan. The complete details behind the Ti:Sa and Verdi systems can be found in the corresponding data sheets [36, 37] and will not be explained further in this thesis.

5.1.2. 684nm Optical Pumping Transition

The 684 nm light to analyze the corresponding transition in dysprosium is produced with a commercial laser diode system[3] giving an output power of 17 mW. The preparation of the laser light itself was done similarly to the setup described in [38]. The setup is shown in figure 5.2. The light is divided in three parts: One part used for the spectroscopy setup, one goes to the Fabry-Perot cavity for frequency calibration and one sent to the wavemeter. The acousto-optical modulator (AOM) in double-pass configuration placed inside the path of the spectroscopy can be used for later experiments to change the frequency of the laser beam even if the laser itself is frequency-stabilized to a spectroscopy resonance.
The overall tuning range of the laser diode is 677 nm-690 nm. Again the interesting dynamic mode-hop-free tuning range is up to around 20 GHz. Tuning the wavelength is done through a scan control included in the control unit of the laser system. More electronic details can be found in the datasheet of the laser [39].

[3] Toptica DL100 pro design

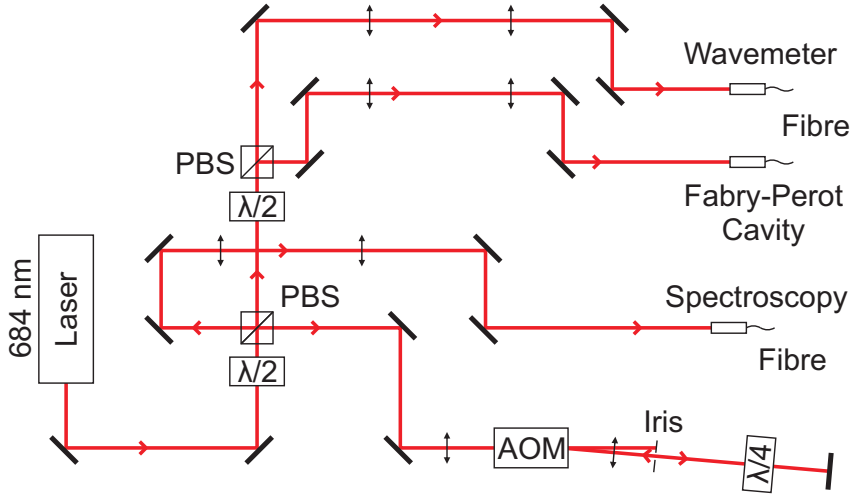

Figure 5.2.: Scheme of the 684 nm laser light preparation. The light coming from the laser head is divided into three parts: one used for the spectroscopy measurements, one going to the fabry-perot cavity and one going to the wavemeter.

5.1.3. Frequency Calibration via Fabry-Perot Interferometer

A common technique to calibrate the frequency scan of a laser is to use a Fabry-Perot interferometer (FPI). Two mirrors with a high reflectivity are standing at a fixed distance. If laser light is sent through this cavity we get a resonance condition for the light depending on its frequency. At the output of the FP cavity we only get constructive interference if the resonance condition is fulfilled. The width of such a resonance peak (full width at half maximum, FWHM) and the distance between two peaks (free spectral

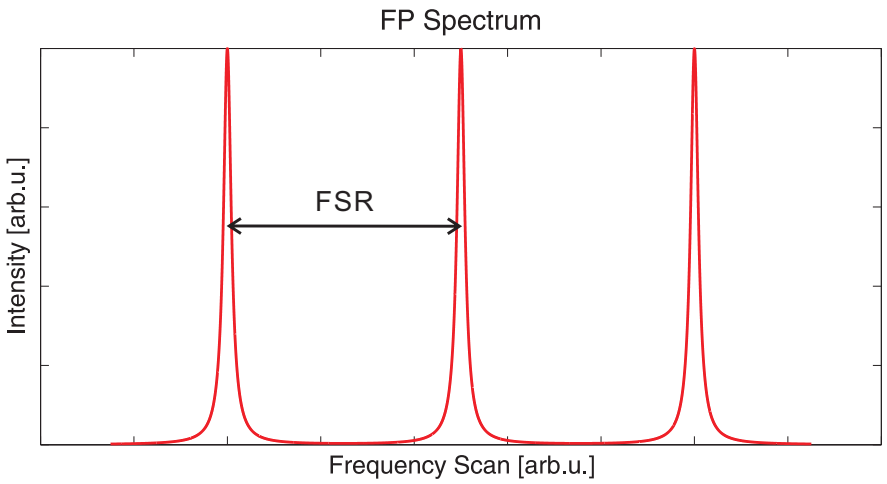

Figure 5.3.: Typical FP spectrum: The intensity is plotted as a function of the frequency scan. Three resonance peaks are visible spaced by the free spectral range (FSR).

range, FSR) are only depending on the reflectivity of the mirrors and the distance between them (see [40]). A FP spectrum can be seen in figure 5.3. As we want to use the FPI for frequency calibration for the spectroscopy measurements we need to characterize it, especially the FSR. For this we use an electro-optical modulator (EOM) creating sidebands at $\nu_{\text{sideband}} = \nu_{\text{laser}} \pm \nu_{\text{mod}}$, where ν_{laser} is the laser frequency and ν_{mod} the modulation frequency applied to the EOM. Those sidebands are fixed in frequency compared to the laser frequency and they will show up as additional peaks in the FP spectrum. With this we characterize the FSR of the FPI and use the FPI spectrum as calibration for a frequency scan during a spectroscopy measurement.

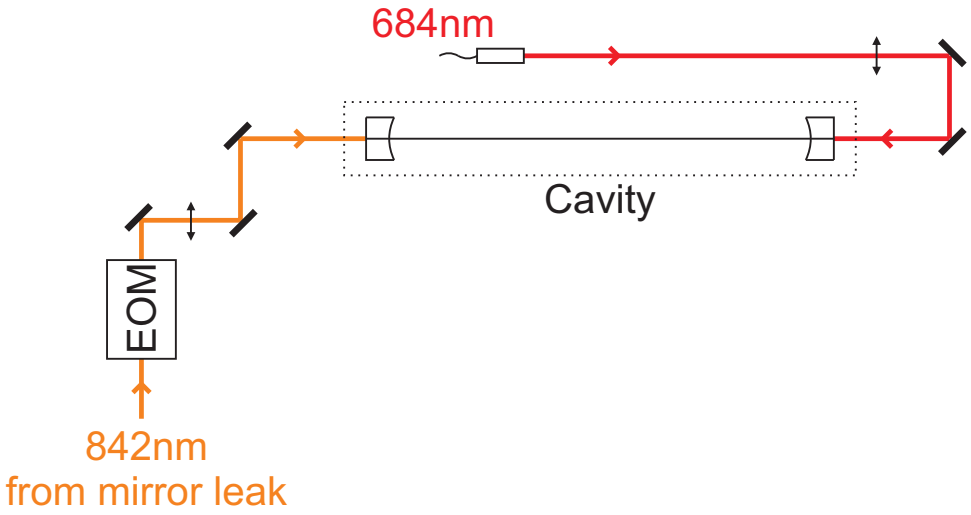

Figure 5.4.: Scheme of the frequency calibration using a FPI in our setup: Both laser beams are focused inside the FP cavity to get a good mode matching. In addition an EOM is placed inside the path of the 842 nm light to create sidebands. Depending on the laser that is used for the measurements, a photo diode is placed behind the cavity to measure the FP spectrum and the other beam is blocked.

In our setup, shown in figure 5.4, the 684nm light is guided with a fiber to the FPI and focused inside the FP cavity to get a good mode matching. In addition, we make use of a leak light coming through a mirror at the output of the Ti:Sa (842 nm) and send this to the same FPI (see figure 5.1). Again this beam is focused inside the cavity in order to have a good mode matching. Depending on which laser is used for the measurements, the other beam is blocked and a photodiode is placed after the cavity to measure the FPI signal. The setup is the same as the one used in [38]. The mirrors are mounted on commercial mirror mounts and as the whole cavity is not placed under vacuum, one has to take care of air fluctuations during a reference scan.

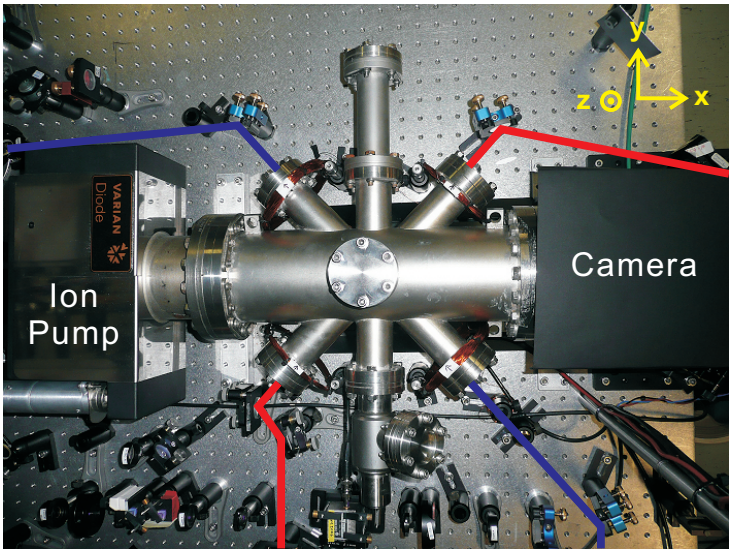

Figure 5.5.: Top view of the vacuum chamber used for the spectroscopy on an atomic beam. The beam paths for the 421nm and the 684nm transitions are shown in blue and red respectively. The effusion oven (not visible on this picture) is mounted below the chamber.

5.2. Spectroscopy on an Atomic Beam

The tunable laser source including a frequency calibration being ready, we now focus on the setup for the spectroscopy itself. During this thesis we tested two different setups for a spectroscopy on an atomic beam. Both use an effusion oven heating up a sample of dysprosium, which is lying in a crucible, to 1250 °C. This leads to a vapor pressure of $p = 0.1\,\mathrm{mbar}$ [24] and we can observe the atomic beam through its fluorescence. To detect this fluorescence we installed a CCD camera[4] to a viewport and thereby check that we have an atomic beam in the chamber. The effusion oven is mounted onto a vacuum chamber reaching a pressure down to $p_{\mathrm{vac}} = 1 \cdot 10^{-9}\,\mathrm{mbar}$. The first setup we used, which will not be further discussed in this thesis, had a few disadvantages[5], which were corrected in the second setup described in the following and shown in figure 5.5. The chamber is built in such a way that four viewports are at the same height as the closure head of the crucible to assure an access to a dense atomic beam. Because of this, we divided the setup into two parts for the optics, which will be described in the following:
Two opposite viewports are used for the spectroscopy of the 421 nm light and the remaining two viewports, which are arranged perpendicular to the first two, for the 684 nm light.

[4] model: pixelfly USB

[5] There were mainly two problems with the setup: The first disadvantage is that the crucible of this oven has a huge hole in the closure head leading to a highly diverging atomic beam. Second, the distance in between the oven and the point where we detect the atoms with the laser beam is about 20cm and, as the atom beam is diverging, the density was too low.

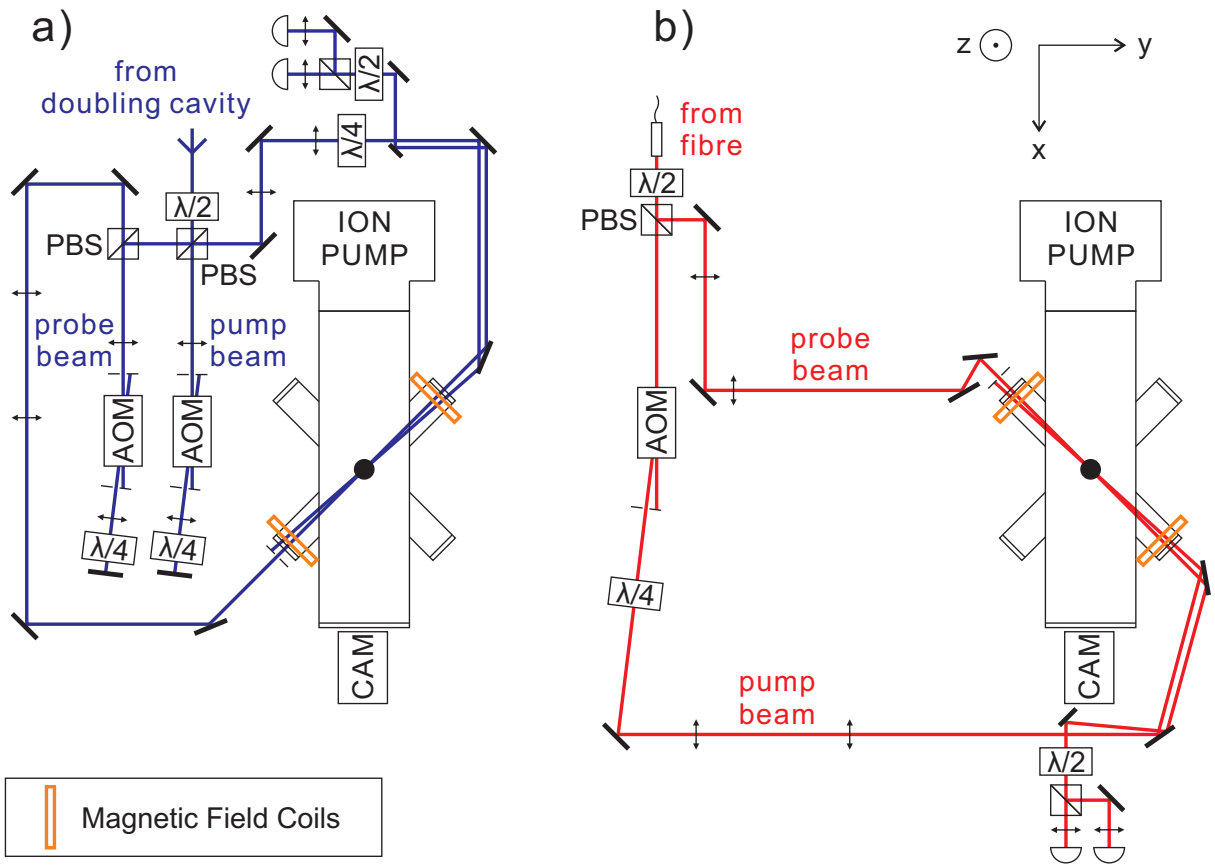

Figure 5.6.: Technical drawing of the setup for the spectroscopy on an atomic beam. a) Setup for the 421 nm cooling transition. b) Setup for the 684 nm optical pumping transition. The overlap of both drawings represent the picture shown in figure 5.5

The setup for the polarization spectroscopy for the 421 nm cooling transition is shown in figure 5.6(a). As already explained in section 4.2.2 the polarization spectroscopy is a Doppler-free spectroscopy method using two counter propagating beams. Therefore the beam coming from the doubling cavity is first divided into two parts with a $\frac{\lambda}{2}$-waveplate and a polarizing beam splitter (PBS). The transmitted part of the beam is used as pump beam, the reflected part as probe beam. Each beam is sent through a double-pass AOM configuration before passing through a telescope in order to magnify the beam size by a factor of four. Both beams are finally sent to the vacuum chamber in a counter propagating way. Additionally, before reaching the chamber, the probe beam goes through a $\frac{\lambda}{4}$-waveplate creating circularly polarized light.
Here we need to have a small angle between the pump and the probe beam as we only want to detect the probe beam in the end. Still there has to be a good overlap between the two beams at the position of the atomic beam. Because of the small angle we can separate both beams and are able to take out the probe beam with a mirror. The transmitted probe beam is divided into two with a $\frac{\lambda}{2}$-waveplate and a PBS. The two beams

are then detected with a light-balancing photodiode system. This system is composed of two separate photodiodes, where the signals are subtracted from each other to give the output signal.
As we already mentioned, the double-pass AOM configuration allows us to fine-tune the frequency offset of the laser beam without changing the frequency of the laser itself. In addition, it allows to tune the intensity of the outcoming beam. This ability is even more important here as we have to chop the intensity of our pump beam in order to use a lock-in amplifier described in section 4.2.1.
The setup for the 684 nm optical pumping light is similar to the one just described for the 421nm light (see figure 5.6(b)). Only the pump beam is passing through an AOM, here in single-pass configuration. Probe and pump beams are then guided through a different pair of viewports of the vacuum chamber as it can be seen in figure 5.6. The detection system of the probe beam is the same as the one discussed for the 421 nm setup.

In addition depending on which setup is used for the measurements we have the ability to connect two different pairs of magnetic field coils creating a small magnetic field at the position of the atoms. Due to the size of the vacuum chamber it was not possible to arrange the coils in a Helmholtz configuration to have a perfectly homogeneous magnetic field. Nevertheless, simulations of the magnetic field show that the homogeneity of the magnetic field is sufficient for our needs. A further discussion of the magnetic field properties will be explained in section 6.3.2.

6. Spectroscopy of the 421nm Cooling Transition

In this chapter we present the results that were obtained on the 421 nm cooling transition. This transition has already been characterized in [20, 23]. Within our precision, we will show that our results match this characterization. We start by presenting the fluorescence spectroscopy and determine the angle of divergence of the atomic beam. We then continue with the saturated absorption spectroscopy and show the dependence of the spectrum on the laser intensity and the temperature of the effusion oven. Finally we present the polarization spectroscopy and how it is depending on the magnetic field.

6.1. Fluorescence Spectroscopy

We first concentrate on the fluorescence spectroscopy of the 421 nm transition, which is shown in figure 6.1. This spectrum was taken using the setup shown in figure 5.6 with an oven temperature of $T_{\text{oven}} = 900\,^{\circ}\text{C}$. For this spectrum, the frequency axis is calibrated through the isotope shift between the two bosons, ^{164}Dy and ^{162}Dy, corresponding to the highest maxima in the spectrum. The isotope shift was measured in ref. [23] to be $\Delta_{164-162} = 913.2\,\text{MHz}$.
The whole spectrum is fitted by a least-square fit using seven Voigt profiles (see equation (3.25)), as we can only observe seven distinct peaks. For this fit, the linewidth of the transition, represented by the Lorentzian profile (see equation (3.20)), was fixed to the natural linewidth: 32.2 MHz [20]. From the fit, we can extract the linewidth of each peak in the spectrum, especially the linewidth of the Doppler-broadened Gaussian profile (see equation (3.24)). In the following, we consider the first peak of the spectrum, assigned to the ^{164}Dy boson. Its measured linewidth is found to be $\omega_{\text{G}} = 165\,\text{MHz} \pm 2\,\text{MHz}$, with the error given by the error of the fit. As discussed in section 3.3.1 this width represents the width of the velocity distribution: the Doppler-width.
From this measurement, one can also extract the diverging angle of the atomic beam, as it is the only reason for the obtained Doppler-width. For this we have to calculate the standard deviation of the transverse velocity distribution. For a Gaussian profile the relation between the $FWHM$ and the standard deviation σ is given by [1]

$$FWHM = 2\sqrt{2\ln 2}\sigma \Rightarrow \sigma = \frac{FWHM}{2.35} = 69.7 \pm 0.7\,\text{MHz}\,. \tag{6.1}$$

[1] The relation can be calculated via Wolfram Mathematica.

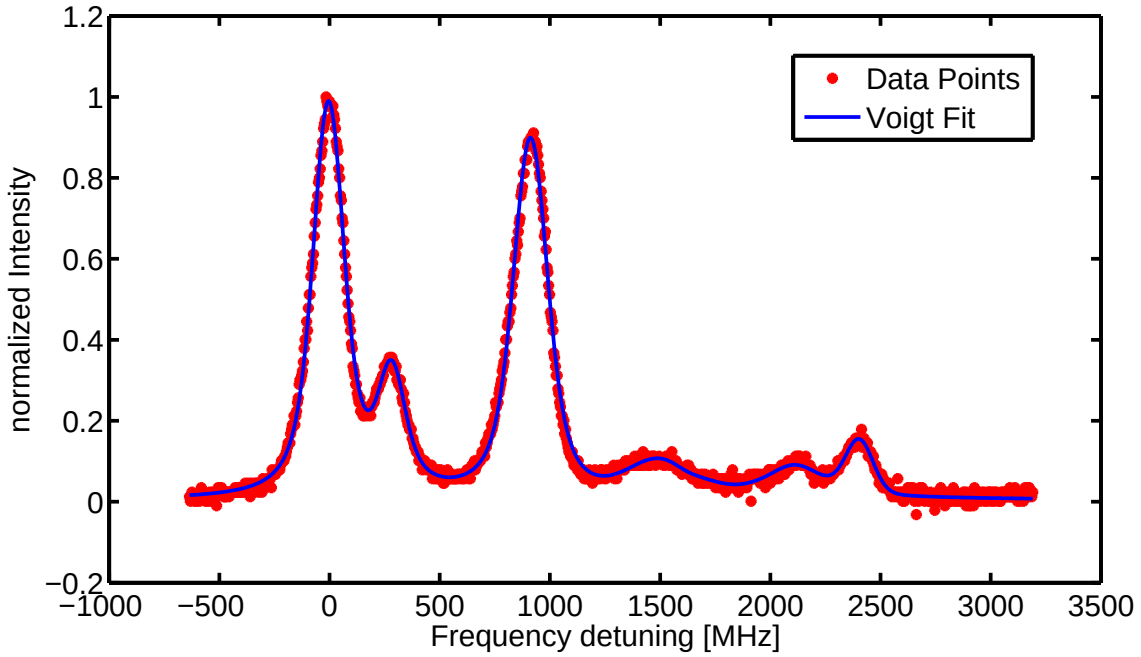

Figure 6.1.: Measured fluorescence signal of the 421 nm transition at an oven temperature of $T_{\text{oven}} = 900\,^{\circ}\text{C}$ shown as red points. A least-square fit was performed using seven Voigt-profiles shown in blue. With the fixed natural linewidth as Lorentzian profile, the fit leads to a Doppler-width of $\omega_{\text{G}} = 165\,\text{MHz}$.

We know that 95.4% of the transverse velocity distribution are in between an interval of $\mu \pm 2\sigma$ and 99.7% are in between an interval of $\mu \pm 3\sigma$, where μ describes the center of the velocity distribution with $v = 0\,\frac{\text{m}}{\text{s}}$. From this we can calculate the maximal transverse velocity component to be

$$v_{2\sigma} = \frac{4\sigma c}{2\nu_0\sqrt{\ln(2)}} = 70.8 \pm 0.7\,\frac{\text{m}}{\text{s}}$$
$$v_{3\sigma} = 106.3 \pm 1.1\,\frac{\text{m}}{\text{s}}\,.$$

With the most probable velocity in the beam direction of $v_{\text{p}}(900\,^{\circ}\text{C}) = 346.5\,\frac{\text{m}}{\text{s}}$ we can calculate the total diverging angle of the atomic beam to be

$$\theta_{2\sigma} = 2\frac{180\,^{\circ}}{\pi}\arcsin\left(\frac{v_{2\sigma}}{v_{\text{p}}}\right) = 23.6 \pm 0.2\,^{\circ} \tag{6.2}$$
$$\theta_{3\sigma} = 35.7 \pm 0.3\,^{\circ}\,. \tag{6.3}$$

In our main chamber we shoot the Zeeman-slower beam counter-propagating to the atomic beam coming from the oven and are able to make a picture of the fluorescence light. From this picture we extract the diverging angle of the fluorescence light to be roughly 31 °,

which is in between the result of the 2σ and the 3σ interval. In addition, we have to consider that here the oven temperature was at $T_{\text{oven}} = 1250\,°\text{C}$. Still the result gives a good approximation.

In addition, in section 4.1.2 we discussed the possibility to measure the lifetime of the excited state through the fluorescence decay when chopping the 421 nm-light using an AOM. As the natural linewidth of the transition was measured to be $\gamma_0 = 32.2\,\text{MHz}$, the lifetime of the excited state is $\tau_e = \frac{1}{2\pi\gamma_0} = 4.94\,\text{ns}$. It is not possible to chop the light with an AOM on this timescale (the typical timescale for chopping is around 100 ns). Furthermore, measuring this time implies that the risetime of the photodiode has to be on the order of about 1 ns or below to be sure that we are not limited by this. Because of this, we measure the linewidth using the saturated absorption spectroscopy, which we describe in the next section.

6.2. Saturated Absorption Spectroscopy

As already described, the fluorescence spectroscopy method does not allow to get a sufficiently high resolution spectrum to resolve all isotopes of dysprosium, including the hyperfine states of the fermionic isotopes. To do so, we therefore performed saturated absorption spectroscopy measurements. A complete spectrum of the isotopes with high natural abundance (see chapter 2) can be seen in figure 6.2(a). The x-axis was calibrated with the Fabry-Perot interferometer, whose signal is shown in figure 6.2(b). The spectrum was taken at an oven temperature of $T_{\text{oven}} = 1250\,°\text{C}$. As we use a lock-in amplifier, we have to chop the intensity of the pump beam. The chopping frequency was chosen to be $f_{\text{chop}} = 50\,\text{kHz}$. The power of the pump beam was measured to be $P_{\text{pump}} = 5\,\text{mW}$, while the probe beam had a power of $P_{\text{probe}} = 1\,\text{mW}$. If we want to compare this to the saturation intensity we need to calculate the peak intensity of the Gaussian beam out of the power and the beam waist w. This is given by the relation $P = \frac{1}{2}\pi I_0 w^2$. If the beam is not perfectly symmetric in x and y-direction we have to replace w^2 with $w_\text{x} w_\text{y}$. In our case the intensity profile of the beam was not perfectly behaving like a Gaussian beam so we only get an estimation for the saturation intensity. The waists for the probe beam were measured to be $w_\text{x} = 1.01\,\text{mm}$ and $w_\text{y} = 0.92\,\text{mm}$. This leads to a peak intensity of the probe beam to $I_{0,\text{probe}} = 68.5\,\frac{\text{mW}}{\text{cm}^2}$ which is slightly above the saturation intensity of the transition $I_{\text{sat}} = 56.4\,\frac{\text{mW}}{\text{cm}^2}$. We can then calculate the expected linewidth using equation (3.32) to be $\gamma_{\text{theo}} = 47.9\,\text{MHz}$. We measured a linewidth for the ^{164}Dy isotope of $\gamma_{164} = 43.1\,\text{MHz}$. Both values are on the same order of magnitude but there is a discrepancy between them. This is coming from the simple picture we used in this calculation. There, we only consider a two-dimensional surface whereas to calculate the linewidth precisely one has to take into account the three-dimensional overlap of the probe and pump beams with the atomic beam. Therefore this is only a rough estimation of the saturation intensities while a more detailed consideration is shown in subsection

6.2.1. The peak intensity of the pump beam, which has a waist of about $w_x = 1.3\,\text{mm}$ and $w_y = 1.87\,\text{mm}$., is calculated the same way and is found to be $I_{0,\text{pump}} = 130.9\,\frac{\text{mW}}{\text{cm}^2}$.

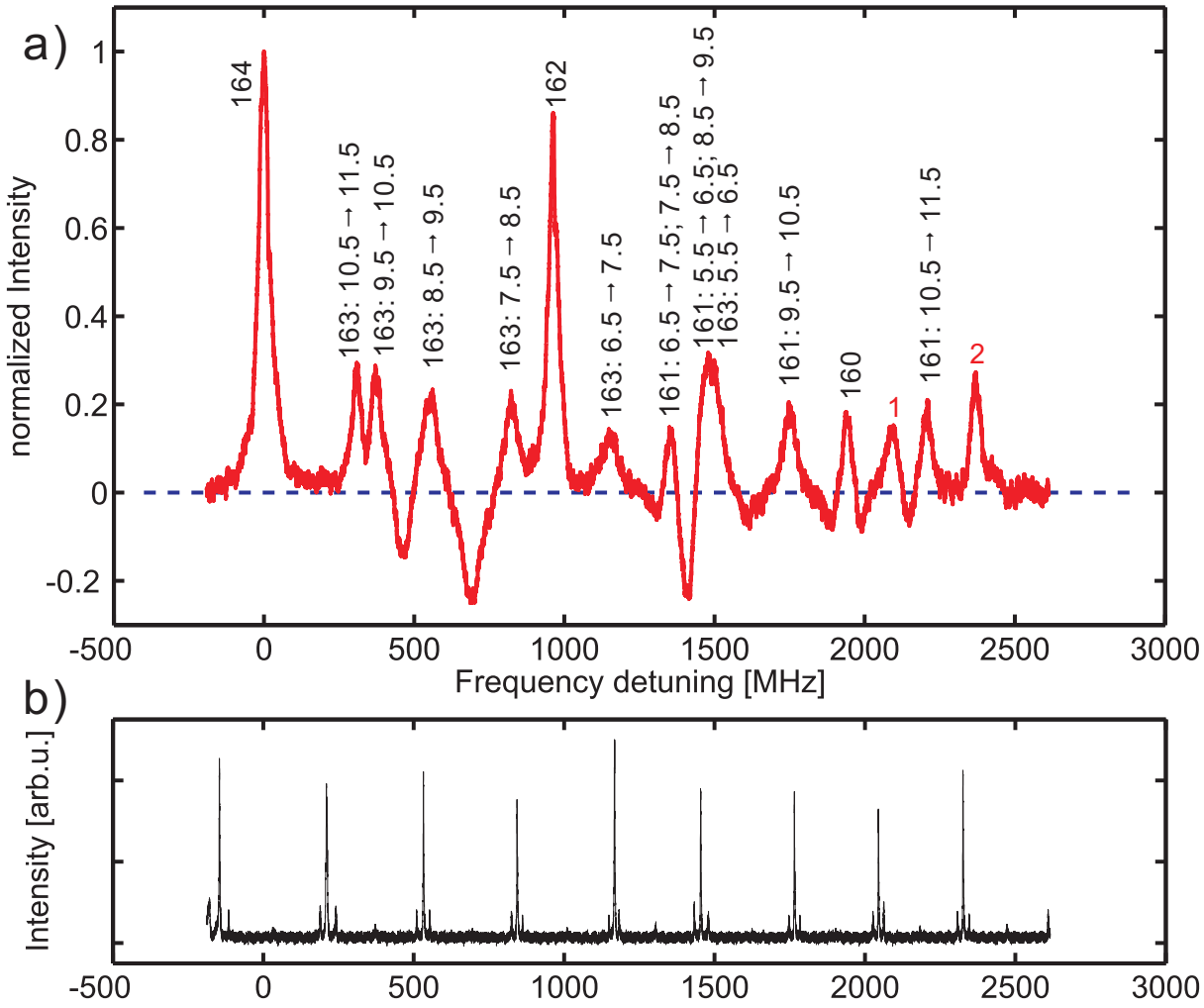

Figure 6.2.: a) Complete spectrum of the highest abundant isotopes of Dy measured using saturated absorption spectroscopy. The red curve represents a single shot with a mean average of 50 points. The zero intensity level is represented by the blue dashed line, showing negative intensity "peaks". Those negative "peaks" in addition to the two peaks named 1 and 2 can be explained by the theory. The labelling "$163 : 10.5 \rightarrow 11.5$" corresponds to the transition of the isotope ^{163}Dy from the hyperfine level $F = 10.5$ in the groundstate to the $F = 11.5$ in the excited state. This also means that both, pump and probe beam, are acting on the same transition. b) Measured Fabry-Perot spectrum during a frequency scan of the Ti:Sa. The FSR was characterized to be 300 MHz.

Assignment of the Transition Peaks

Let us take a closer look at the spectrum: Two prominent peaks appear at a relative frequency $\nu_{164} = 0\,\text{MHz}$ and at $\nu_{162} = 962.6\,\text{MHz}$. As already indicated, those two transition peaks correspond to the ^{164}Dy and ^{162}Dy bosons. In addition to those two strong peaks we find several smaller peaks, which were identified with the ^{160}Dy boson at a relative frequency of $\nu_{160} = 1938\,\text{MHz}$ and with hyperfine states of the ^{161}Dy and ^{163}Dy fermions. Out of those values we can calculate the isotope shifts between the three most abundant bosons and compare them to the results given in [23] (see table 6.1).

	$\delta\nu_{164-162}$ [MHz]	$\delta\nu_{164-160}$ [MHz]	$\delta\nu_{162-160}$ [MHz]
our measurements	-962.6	-1938	-975.4
measurements done in [23]	-913.2(8)	-1895(2)	-981.8(28)
difference	49.4	43	-6.4

Table 6.1.: Isotope shifts of the three highly natural abundant bosonic isotopes compared to the measurements done in [23].

We can see that the isotope shifts differ slightly from the results obtained in [23]. This is mainly due to the fact that the frequency ramp of the Ti:Sa is not perfectly linear. This can also be seen in the Fabry-Perot signal through the irregular distance between the transmission peaks.
The fermionic hyperfine transitions could be identified using equation (3.13) with the excited state (A, B) coefficients from [23] and the ground state (A, B) coefficients from [41]. As this is a $J \to J+1$ transition, the strongest transitions are the ones going from $F \to F+1$. The notation of those transitions is chosen in a way that e.g. "$163 : 10.5 \to 11.5$" corresponds to a transition for the ^{163}Dy isotope from the groundstate $F = 10.5$ to the excited state $F = 11.5$.

Experimental Observation of Unexpected Effects

We see two interesting effects in the spectrum that have to be explained: first, we see two additional peaks, marked as 1 and 2, that are not explained by the model so far. Second, we obtain negative intensities within the spectrum.

- To explain the appearance of the two additional peaks, we first need to have a closer look to the way how this spectrum was measured. The easiest way to see this is in the picture of population number of the states. With an oven temperature of $T_{\text{oven}} = 1250\,^{\circ}\text{C}$, we can assume having the same population in every F hyperfine state: $N_{5.5} = N_{6.5} = ... = N_{11.5} = N$. If the pump beam is resonant to the transition $161 : 9.5 \to 10.5$ it will excite 50% of the atoms to the excited $F = 10.5$ state. If the probe beam is resonant to the same transition it will completely be transmitted and we detect this as a peak in the spectrum. This situation is shown in figure 6.3(a) and relates to the saturated absorption

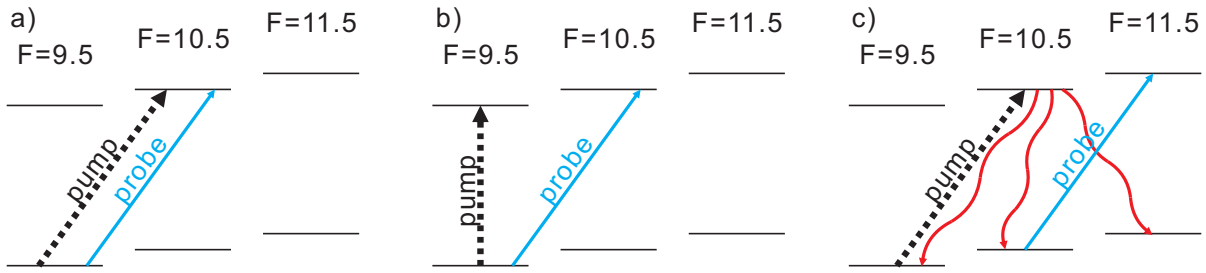

Figure 6.3.: Part of the hyperfine excitation spectrum of pump and probe beams for fermionic Dy. The pump beam is chopped with an AOM indicated as dashed black arrow, the probe beam is shown in blue. a) Both beams are acting on the same hyperfine transition. This leads to transmission peaks in the spectrum. b) Pump and probe beams are acting on the same groundstate but adress different excited states. This leads to additional peaks in the spectrum. c) Both beams are acting on different states. The spontaneous decay to the allowed groundstates is shown as curved red arrows. This effect leads to negative intensities in the spectrum.

spectroscopy prescribed in section 4.2.1.
As pump and probe beams are linearly polarized we are not only exciting $F \rightarrow F+1$ transitions but also $F \rightarrow F$ or $F \rightarrow F-1$. So let us assume the situation shown in figure 6.3(b), where the pump beam is resonant to the transition $161 : 9.5 \rightarrow 9.5$ and the probe beam is resonant to $161 : 9.5 \rightarrow 10.5$. In this situation we need to consider that we use a lock-in amplifier and a chopped pump beam. If the intensity of the pump beam is zero, we excite the transition $161 : 9.5 \rightarrow 10.5$ due to the probe beam, leading to population of $N_{\mathrm{g},9.5} = N_{\mathrm{e},10.5} = \frac{N}{2}$. If the pump beam is at its full intensity, the population of the $F = 9.5$ groundstate changes as the pump beam is depopulating this state to the $F = 9.5$ excited state. Considering this, there are less atoms in the $F = 9.5$ groundstate that can be excited by the probe beam. Using this simple picture we directly see that the transmission of the probe beam will be higher if the pump beam is at its full intensity compared to a pump beam with zero intensity. This difference in transmission will then also lead to a peak in the spectrum.
We can calculate theoretically the frequency where this peak should appear related to the ^{164}Dy transition with the equation (3.13). The shift in the case of the example given above is calculated to be $\delta\nu_1 = 2056\,\mathrm{MHz}$. This represents the peak, marked as 1, in figure 6.2. Here the shift to the ^{164}Dy transition was measured to be $\delta\nu_1 = 2096\,\mathrm{MHz}$. The same calculation can be done for the second peak, marked as 2, with a measured frequency shift of $\delta\nu_2 = 2370\,\mathrm{MHz}$. This is fitting to the theoretical calculation if the probe beam is resonant on the $161 : 10.5 \rightarrow 11.5$ transition and the pump beam is resonant with the $161 : 10.5 \rightarrow 10.5$ transition. The calculated value for this shift is $\delta\nu_2 = 2333\,\mathrm{MHz}$. The difference between the theoretical calculated shift and the measured shift is again due to the non-linear frequency scan of the Ti:Sa system. We do not observe all of these crossed transitions as most of them are either not in the range of the scan or are sitting on top of another transition.

- The negative intensities are explained in a similar way, using the scheme shown in figure 6.3(c). In this example the probe beam is resonant to the $161 : 9.5 \rightarrow 10.5$ transition, while the probe beam is resonant with the $161 : 10.5 \rightarrow 11.5$ transition. We now have a look at the atoms in the $F = 10.5$ excited state. Within the lifetime of the excited state those atoms decay back to the groundstate. Here they can decay back to the $F = 9.5$ groundstate but also to the states $F = 10.5$ and $F = 11.5$. We now again have to compare the transmission of the probe beam depending on the power of the pump beam. With no pump beam, we recover the case just described above. With the pump beam at its full intensity we see that the population in the $F = 10.5$ groundstate is higher compared to the case with no pump beam. With a higher population, more atoms can be excited by the probe beam, which leads to a lower transmission of the probe beam. This lower transmission corresponds to a dip in the spectrum and the position of those dips can also be confirmed by theoretical calculations.

6.2.1. Dependence on the Laser Intensity

Now that we understand the shape of our spectroscopy signal, we want to measure the effect of the laser intensities of probe and pump beam on this signal. For this study, we consider only the ^{164}Dy isotope as this has the highest natural abundance and look at the linewidth and the absolute intensity of the corresponding peak.

Effect of the Laser Intensity on the Linewidth

We first look at the linewidth depending on the power of the probe beam shown in figure 6.4. This study is performed as a function of three different powers for the pump beam: $P_{\text{pump}} = 17\,\text{mW}$, $P_{\text{pump}} = 11\,\text{mW}$ and $P_{\text{pump}} = 5\,\text{mW}$. Here, the lines always correspond to a fit to the data points following equation (3.32). The error for the linewidth is given by a statistical error out of three measurements. The error on the probe power is coming from the fact that the laser was not perfectly stable over one scan and therefore the error considers the maximal deviation to the set value.
The first observation is that the data points follow the theory described by equation (3.32), where the natural linewidth γ_0 and the saturation parameter S were set as fit parameters. As a consequence, the fit gives the minimal linewidth γ_{min} that can be achieved with the pump beam power that we use. If we take a look at the measurement with a pump power of $P_{\text{pump}} = 5\,\text{mW}$ we find a minimal linewidth of $\gamma_{\text{min}} = 30.87 \pm 0.27\,\text{MHz}$, where the error is given by the fit. This value is smaller than the natural linewidth of the transition, measured in [20] to be $\gamma_0 = 32.2\,\text{MHz}$. This discrepancy is again due to the calibration of the frequency axis. As already mentioned, the ramp of the frequency scan of the Ti:Sa is not linear, leading to deviations in the FP signal. In this signal, the deviation of the FSR is up to $\Delta_{\text{FSR}} = 15\,\text{MHz}$ within one free spectral range of $\text{FSR} = 300\,\text{MHz}$. If we assume that this error is linear within one FSR, we can estimate an offset to the measured

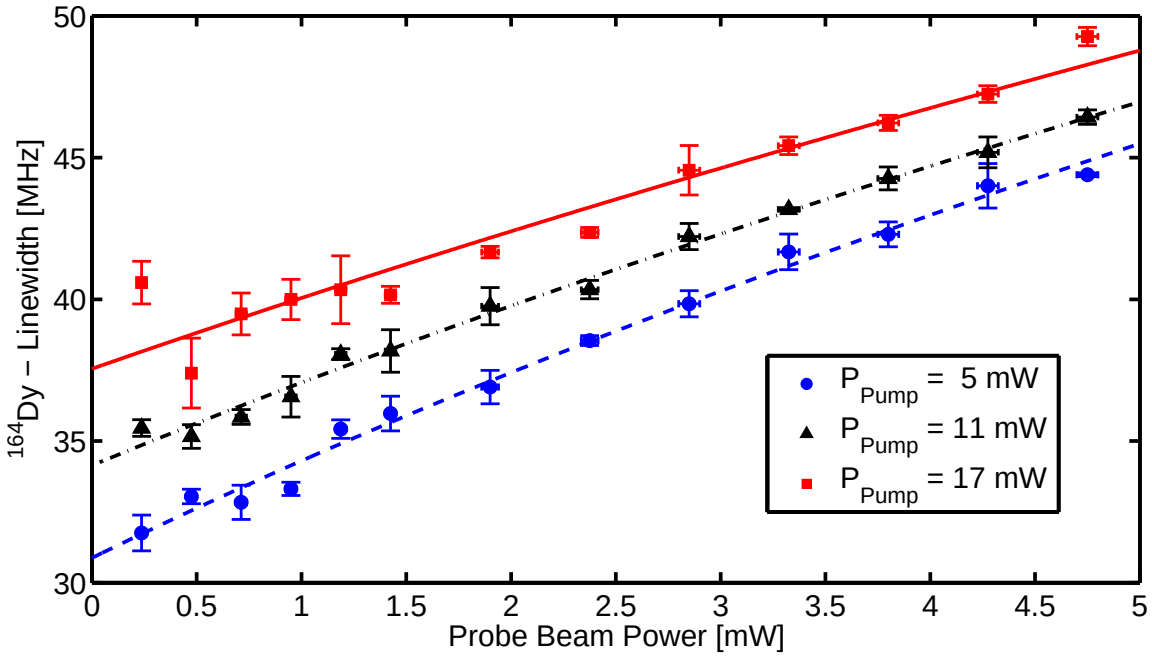

Figure 6.4.: Dependence of the linewidth on the power of the probe beam for three different powers in the pump beam: $P_{\text{pump}} = 17\,\text{mW}$ (red square), $P_{\text{pump}} = 11\,\text{mW}$ (black triangle) and $P_{\text{pump}} = 5\,\text{mW}$ (blue circle). The linewidth is extracted from a lorentzian fit to the ^{164}Dy peak. The lines correspond to a fit of the data points following equation (3.32). The errorbars on the measured linewidth corresponds to a statistical error given by three different measurements. The error in the power of the probe beam is due to a drift of the power during a measurement.

linewidth of $\gamma_{\text{off}} \approx 1.5\,\text{MHz}$. If we take this offset into account, the minimal linewidth becomes $\gamma_{\text{min}} \approx 32.4 \pm 1.6\,\text{MHz}$ and we therefore recover the natural linewidth.
From the fit, we can also extract the saturation power of the probe beam. As this measurement is directly performed with the atoms it already takes into account the overlap of the two beams with the atomic beam. For the measurement with $P_{\text{pump}} = 5\,\text{mW}$ we observe a saturation power of $P_{\text{sat}} = 4.27 \pm 0.21\,\text{mW}$.
A second observation is that both, the minimal linewidth and the saturation power of the probe beam are depending on the power of the pump beam and shift to higher values for higher pump power. This effect can be understood if one considers that the probe beam has to saturate a linewidth broadened by the pump power. This means that there one has to distinguish between the saturation intensity given by the natural linewidth and the intensity we can extract from the fit. This intensity is related to the broadened linewidth by the pump beam and not to the natural linewidth of the transition. The results for the three different measurements are shown in the table 6.2.

	$P_{\text{pump}} = 5\,\text{mW}$	$P_{\text{pump}} = 11\,\text{mW}$	$P_{\text{pump}} = 17\,\text{mW}$
γ_{min}	$30.87 \pm 0.27\,\text{MHz}$	$34.14 \pm 0.21\,\text{MHz}$	$37.55 \pm 0.58\,\text{MHz}$
P_{sat}	$4.27 \pm 0.21\,\text{mW}$	$5.59 \pm 0.22\,\text{mW}$	$7.27 \pm 0.86\,\text{mW}$

Table 6.2.: Minimal linewidth and saturation power of the 421 nm transition for different pump powers. The values are extracted from the three different measurements shown in figure 6.4 and are given without the offset correction (see text).

The broadening effect of the pump beam on the linewidth can be seen in figure 6.5. The power of the pump beam was varied while the power of the probe beam was fixed to $P_{\text{probe}} = 0.25\,\text{mW}$. Again the data follow the theory and we can extract both the minimal linewidth and the saturation power:
- The minimal linewidth is found to be $\gamma_{\text{min}} \approx 28.69 \pm 0.39\,\text{MHz}$, which is below the natural linewidth of the transition. The difference is again explained by the non-linear ramp of the Ti:Sa frequency scan. We estimated this error to be $\gamma_{\text{off}} \approx 1.5\,\text{MHz}$. In fact, this is only true if we consider the error to be linear over the scan. In this sense, this offset error is the mean value of the FSR error in between two resonance peaks. However, the non-linearity may vary within one FSR, which cannot be seen in the FP signal itself.
- In addition, we find a saturation power for the pump beam of $P_{\text{sat}} = 19.42 \pm 1.56\,\text{mW}$.

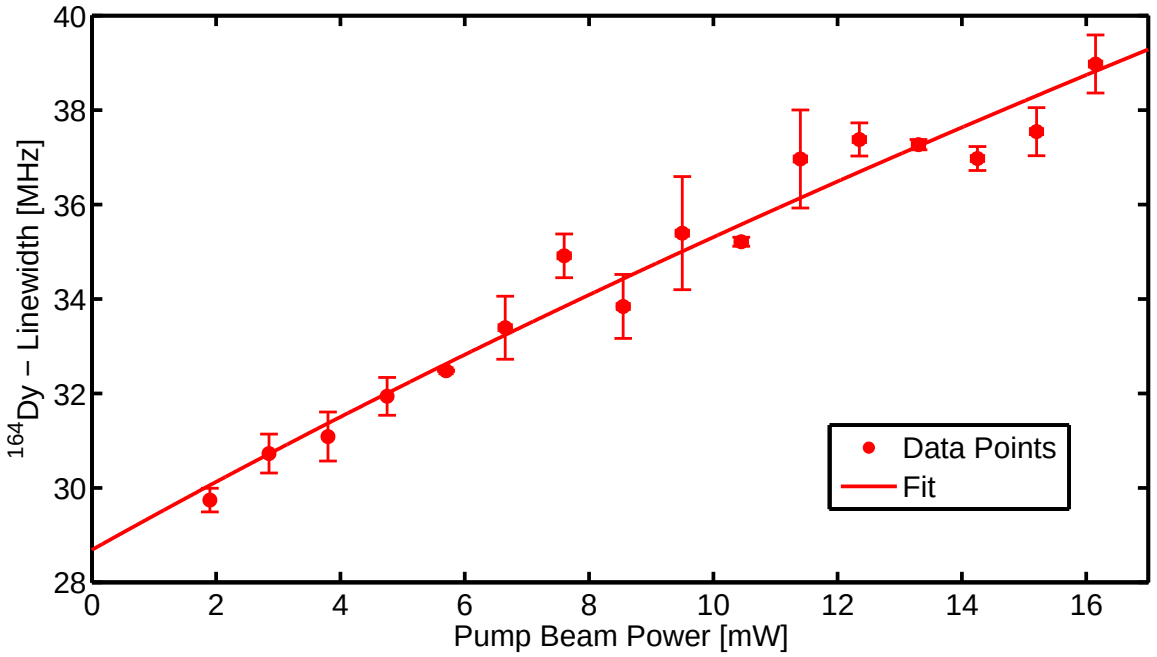

Figure 6.5.: Dependence of the measured linewidth on the power of the pump beam. The power of the probe beam was fixed to $P_{\text{probe}} = 0.25\,\text{mW}$. The errorbars correspond to a statistical error from three different measurements. The solid line corresponds to a fit following equation (3.32).

Effect of the Laser Intensity on the Peak Amplitude

The laser intensity also affects the amplitude of the measured transition peaks. We expect the peak amplitude to increase linearly with increasing **probe beam power**. This behavior is nicely shown in figure 6.6. The peak amplitude in mV is the voltage that was given by the photodiode and points out the need of a lock-in amplifier. We see that the slope of this linear behavior is also increasing with increasing power of the pump beam.
We also measure the effect of the **pump beam power** on the peak amplitude (see figure 6.7) and observe, as expected, a non-linear behavior as already discussed in section 3.3.2. Considering that the probe beam is probing the population difference of the involved states we fit the data points with equation (3.34), which give the dependence of the excited state population onto the power of the excitation laser beam. With this fit, we can again measure the saturation power for the pump beam to be $P_{\text{sat}} = 15.38 \pm 2.82\,\text{mW}$. Within the errorbar of this value and the one calculated from the linewidth dependence ($P_{\text{sat}} = 19.42 \pm 1.56\,\text{mW}$) we can find an average at around $P_{\text{sat}} = 18.5 \pm 3.2\,\text{mW}$, giving a good approximation for the saturation power.

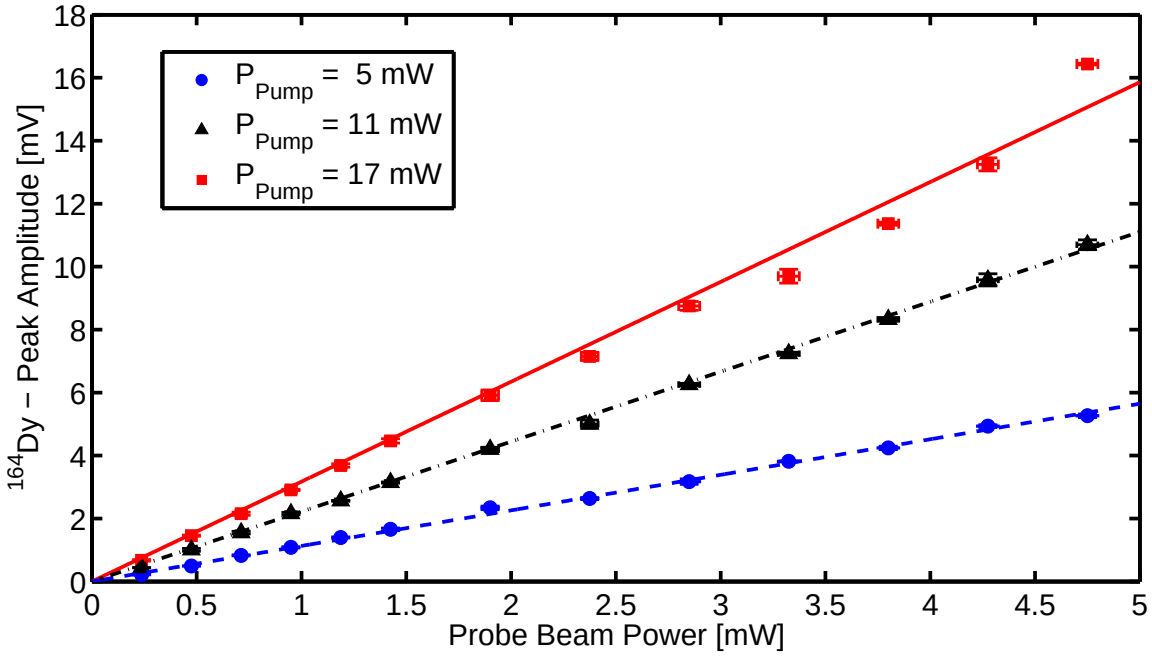

Figure 6.6.: The dependence of the peak amplitude to the power of the probe beam for three different powers in the pump beam: $P_{\text{pump}} = 17\,\text{mW}$ (red square), $P_{\text{pump}} = 11\,\text{mW}$ (black triangle) and $P_{\text{pump}} = 5\,\text{mW}$ (blue circle). The errorbars are a statistical error for three different measurements. The solid line represents a linear fit to the data points.

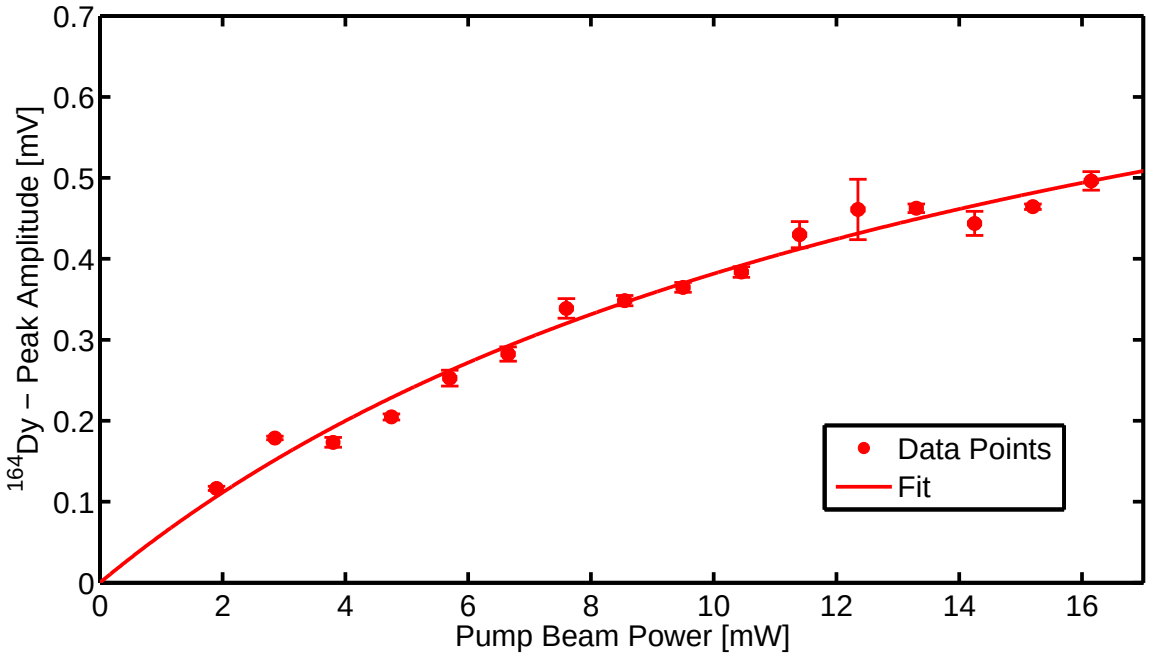

Figure 6.7.: The dependence of the peak amplitude to the power of the pump beam is shown. Here, the power of the probe beam was fixed to a value of $P_{\text{probe}} = 0.25\,\text{mW}$. The errorbars are a statistical error for three different measurements. A fit following to equation (3.34) is shown as solid line.

6.3. Polarization Spectroscopy

We discuss the observation of a spectroscopy signal and its dependence on the magnetic field and the temperature of the effusion oven in this section. From the results of the saturated absorption spectroscopy we set the power of the probe beam to $P_{\text{probe}} = 0.25\,\text{mW}$ and the power of the pump beam to $P_{\text{pump}} = 5\,\text{mW}$ as this delivered a good compromise between signal strength and linewidth.
A complete polarization spectroscopy signal is shown figure 6.8. We see that we cannot observe all hyperfine transitions of the ^{161}Dy and the ^{163}Dy fermionic isotopes but only the strongest ones. In addition, we cannot observe any ^{160}Dy peak. We see however that the shape of the signal is similar to the one discussed in section 4.2.2. As we want to use this signal to frequency lock the laser to one of the zero crossings, we need to have a look at the frequency root mean square (ν_{RMS}). To estimate the ν_{RMS}, we first have a look at the intensity RMS (i_{RMS}) of the signal in the region where the signal should be zero, e.g. for a frequency above $\nu = 1750\,\text{MHz}$. The i_{RMS} of this area is calculated[2] to be $i_{\text{RMS}} = 0.0235$.
We fit the slope m of the ^{164}Dy error signal with a linear function to be $m = 0.038\,\frac{1}{\text{MHz}}$.

[2]The i_{RMS} does not have a unit as it was calculated within the normalized intensity.

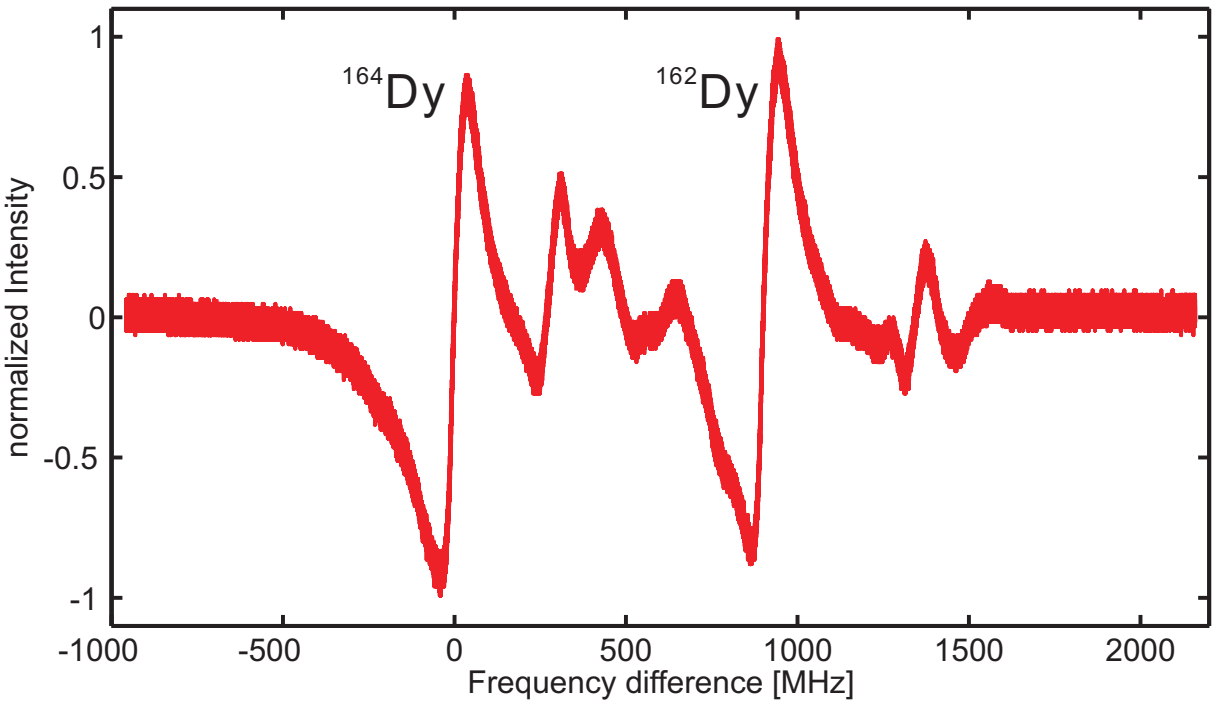

Figure 6.8.: Polarization spectroscopy signal, obtained in a single shot measurement.

With this we can calculate the ν_{RMS} and find $\nu_{\mathrm{RMS}} = \frac{i_{\mathrm{RMS}}}{m} = 0.61\,\mathrm{MHz}$. Following this, we can frequency-lock the laser on a short timescale to the transition within a resolution of $\nu_{\mathrm{RMS}} = 0.61\,\mathrm{MHz}$. Compared to the natural linewidth of the transition, which is $\gamma_0 = 32.2\,\mathrm{MHz}$, we can frequency-lock the laser to the center frequency with a precision of 1.9%.
As the properties of the spectrum concerning probe and pump beam power have already been discussed in section 6.2 we want to focus on the dependence on the temperature of the effusion oven and the magnetic field in the following subsections.

6.3.1. Dependence on the Oven Temperature

We focus here on the dependence of the polarization spectroscopy signal on the oven temperature. The temperature of the effusion oven changes the vapor pressure of the Dy and therefore the flux of the Dy atomic beam. The linewidth is not depending on the number of atoms and we only see a change on the slope of the error signal and the peak amplitude. As the vapor pressure is depending on the temperature following the Antoine equation [42], we fit the slope and the amplitude with this equation. The dependence of the slope on the oven temperature is shown in figure 6.9. Furthermore, the dependence of the amplitude on the oven temperature is shown in figure 6.10. We see that both the amplitude and the slope follows the theory of the Antione equation.

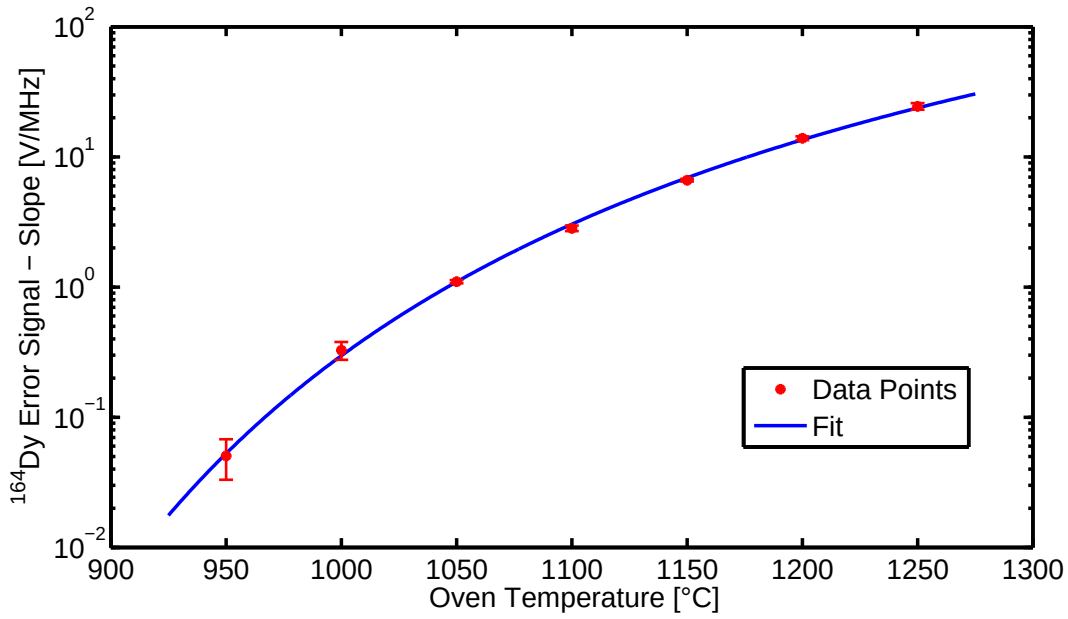

Figure 6.9.: Dependence of the slope on the temperature. The data points were fitted with the Antoine equation from [42]. The errorbars are a statistical error for three different measurements.

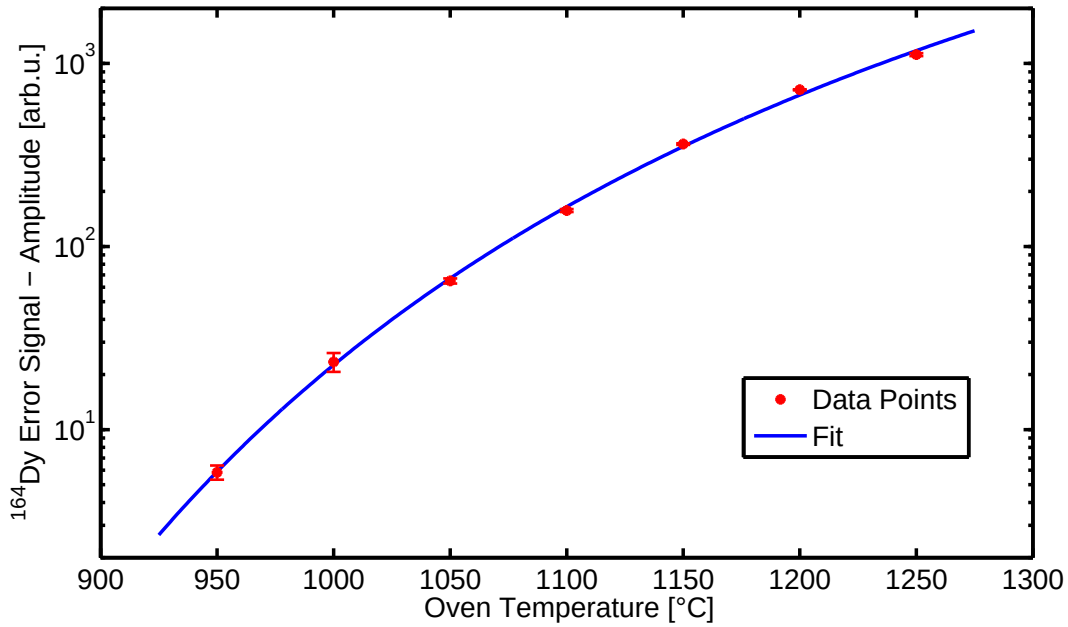

Figure 6.10.: Dependence of the amplitude on the temperature. The data points were fitted with the Antoine equation from [42]. The errorbars are a statistical error for three different measurements.

6.3.2. Dependence on the Magnetic Field

We finally want to investigate a dependence of the polarization spectroscopy signal on an applied magnetic field. As discussed in section 4.2.2, if the magnetic field is applied along the propagation axis of the excitation laser we expect the amplitude to increase linearly with the strength of the magnetic field. Experimentally we observe the behavior shown in figure 6.11.

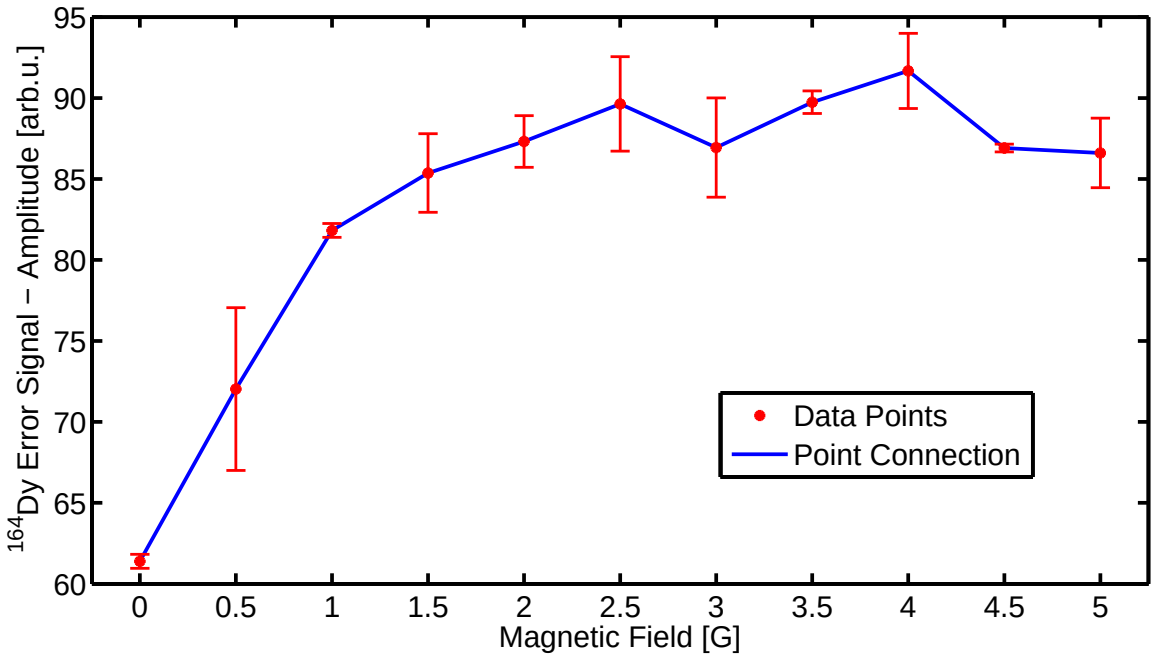

Figure 6.11.: The figure shows the dependence of the amplitude on the magnetic field. The errorbars are a statistical error for three different measurements. The blue line is just a guide to the eye as we did not consider any theory here.

We can see that the amplitude is first increasing linearly, as we expect it to do by defining a quantization axis, but saturates already at a magnetic field of around $B = 2\,\mathrm{G}$. We think that here the magnetic field is already strong enough to define the quantization axis.
However, to create a fully polarzied atomic sample, we need to have a magnetic field strength on the order of the kinetic energy of the atomic beam:

$$\mu_\mathrm{B} B = \frac{1}{2} m_\mathrm{Dy} v_\mathrm{p}^2 \,, \tag{6.4}$$

With the atomic mass of dysprosium m_Dy and the most probable velocity v_p given by the temperature of the oven. Here we would find that the magnetic field has to be around $B = 10^7\,\mathrm{G}$, so eight orders of magnitude higher than the field we applied. Even with this rough estimation, we can tell that this is not the right explanation for the saturation.

Another explanation could be that there is some undefined magnetic field in the chamber, which is e.g. coming from the ion pump and which can only be estimated.
Still, this measurement shows that a magnetic field of around $B = 2\,\mathrm{G}$ is already sufficient to saturate the amplitude of the polarization spectroscopy signal in our setup.

7. Spectroscopy of the 684nm Optical Pumping Transition

In this chapter we discuss the results obtained with different spectroscopy methods on the 684 nm transition. This transition is only partly known and so far the linewidth was only roughly estimated to $\gamma_{684} = 50 - 350\,\mathrm{kHz}$ (see appendix A.2). We also present a measurement to determine the hyperfine structure of the excited state and a direct measurement of the excited state lifetime.

7.1. Saturated Absorption Spectroscopy

Knowing the natural linewidth of a transition, we can calculate the corresponding saturation intensity. If we consider the boundary values of the estimation of γ_{684} we find a rough estimation of the saturation intensity [26]

$$I_\mathrm{S} = \frac{hc\,\gamma_{684}}{6\lambda^3} = 0.52\,\frac{\mu\mathrm{W}}{\mathrm{cm}^2} \cdots 3.62\,\frac{\mu\mathrm{W}}{\mathrm{cm}^2}\,. \tag{7.1}$$

This would mean that with a beam with a waist of $w = 1\,\mathrm{mm}$ and a power of $P \approx 0.06\,\mu\mathrm{W}$, this transition is already saturated. In our measurements, a power of $P \approx 100\,\mu\mathrm{W}$ leads to a signal-to-noise ratio of one. As a consequence, we cannot extract the linewidth from the saturated absorption spectroscopy. Nevertheless, the broadened linewidth still allows to record a spectrum of the transition, shown in figure 7.1. It was taken at an oven temperature of $T_\mathrm{oven} = 1250\,^\circ\mathrm{C}$ with a pump beam power of $P_\mathrm{pump} = 2.8\,\mathrm{mW}$ and a probe beam power of $P_\mathrm{probe} = 1.1\,\mathrm{mW}$. Additionally, the data is averaged over 100 single shots. With such a high power in both beams we expect the linewidth to be broadened and we measure $\gamma = 8.5\,\mathrm{MHz}$ for the strongest peak.
Out of this spectrum we extract the frequency shift from each peak compared to the strongest peak, in order to assign them. If we take a closer look to the arrangement of the peaks we can already extract some information: clearly, the two strong peaks are related to the ^{162}Dy and the ^{164}Dy isotopes. In addition, in between those two peaks we expect hyperfine transitions of the ^{163}Dy isotope. This already gives a rough order of the isotopes for the calculations.

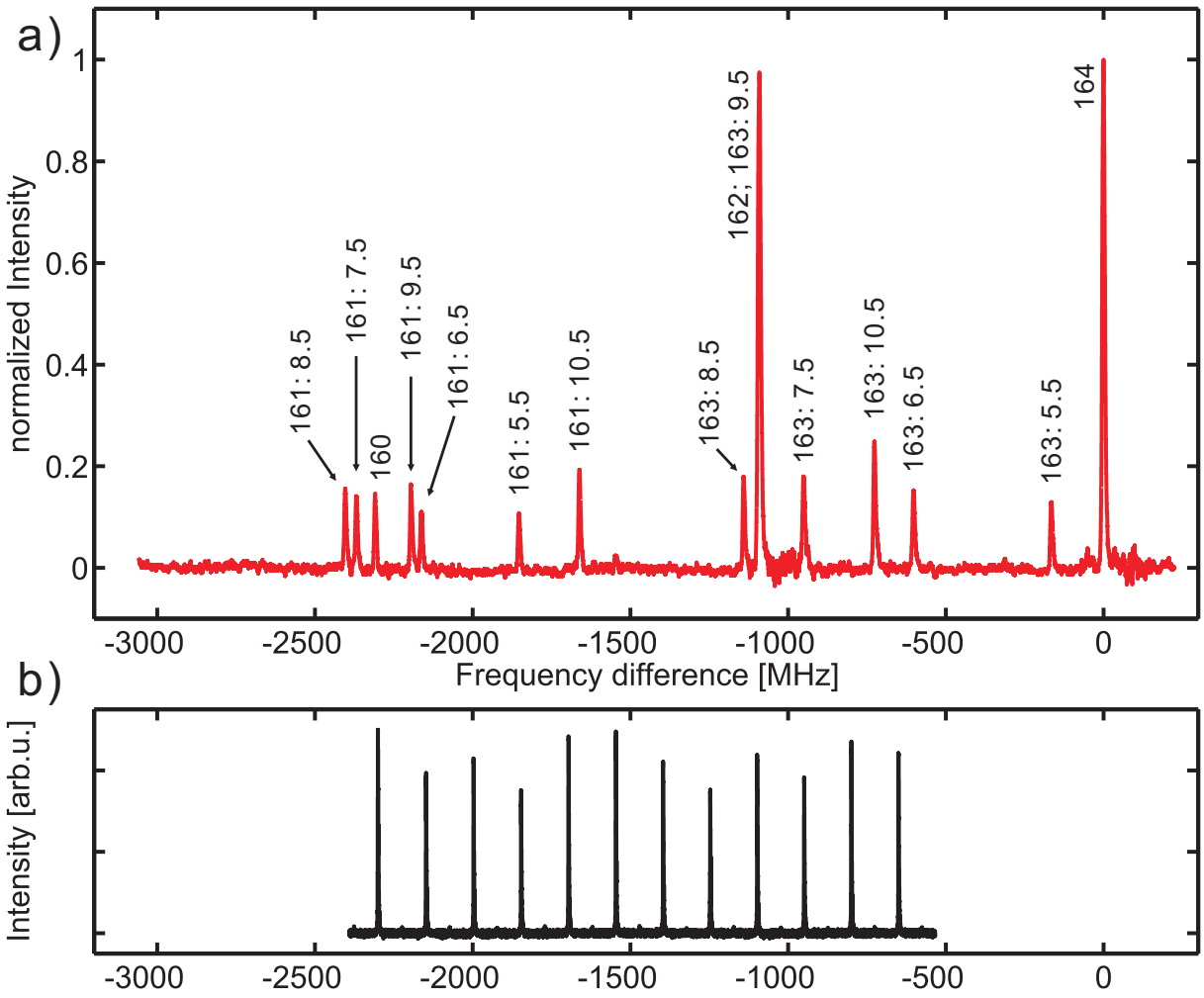

Figure 7.1.: a) Complete spectrum of the highest abundant isotopes of Dy measured using saturated absorption spectroscopy. The normalized intensity is plotted against the frequency difference to the highest peak (^{164}Dy). The data is averaged over 100 single pictures. Here, the labeling "163 : 10.5" corresponds to a transition for the isotope ^{163}Dy from the hyperfine level $F = 10.5$ in the groundstate to the $F = 10.5$ in the excited state. b) Measured FP spectrum during a frequency scan of the Ti:Sa. The FSR was characterized to be 150 MHz.

7.2. Assignment of the Fermionic Hyperfine Transitions

We made the assignment of the peaks, taking into account equations (3.13) and (3.12)

$$\Delta\nu = (A_\mathrm{e} - A_\mathrm{g})K + (B_\mathrm{e} - B_\mathrm{g})\frac{\frac{3}{2}K(2K+1) - I(I+1)J(J+1)}{2I(2I-1)J(2J-1)} - \nu_\mathrm{iss}\,, \tag{7.2}$$

where (A_e, B_e) are the coefficients for the excited state, (A_g, B_g) are the coefficients for the groundstate [41] and ν_iss is the isotope shift in the excited state. As the transition is

a $J \rightarrow J$ transition, we expect the strongest transitions to be the $F \rightarrow F$ ones leading to six hyperfine transitions for each fermion. This means we have a set of six equations with three unknown variables: A_e, B_e and ν_{iss}. To get these we solve the equations for three measured shifts and recalculate the shifts for the remaining three. When the calculated shifts match the three remaining measured shifts we determined the coefficients:

	A_e [MHz]	B_e [MHz]	ν_{iss} [MHz]
^{161}Dy	-108.95	2249.66	2100.63
^{163}Dy	152.55	2352.61	821.72

Table 7.1.: (A, B) hyperfine coefficients and isotope shifts of the excited state of the 684 nm transition for the fermionic Dy isotopes.

We see that the ratios in between the excited state coefficients of the two fermionic isotopes $\frac{A_e(163)}{A_e(161)} = -1.4002$ and $\frac{B_e(163)}{B_e(161)} = 1.0458$ are close to those from the groundstate $\frac{A_g(163)}{A_g(161)} = -1.4003$ and $\frac{B_g(163)}{B_g(161)} = 1.0561$. This shows that there is no hyperfine anomaly for this transition, similarly to [43].
With these values we can assign the peaks shown in figure 7.1 leading to the following table 7.2:

F	measured shift [MHz]	calculated shift [MHz]
^{163}Dy		
5.5	165.18(4)	**165.18**
6.5	601.94(4)	601.98
7.5	950.34(4)	947.99
8.5	1140.49(3)	1136.66
9.5	1091.08(1)	**1091.08**
10.5	725.76(3)	**725.76**
^{161}Dy		
5.5	1852.26(6)	**1852.26**
6.5	2162.18(6)	**2162.18**
7.5	2368.10(5)	**2368.10**
8.5	2403.38(5)	2404.62
9.5	2194.75(4)	2197.91
10.5	1661.15(3)	1665.44

Table 7.2.: Comparison of the measured frequency shifts between the hyperfine transitions of the fermionic isotopes with the values calculated from (A, B) coefficients and isotope shifts. The error on the measured values is coming from the position error of a multiple Lorentzian fit to the spectrum. The values shown in bold represent the three values used to solve the equations. The three remaining are the ones calculated with the coefficients from table 7.1.

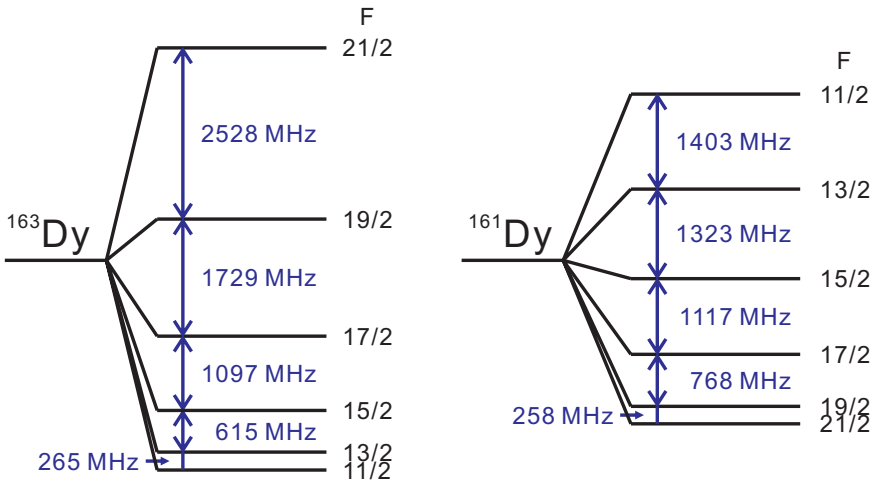

Figure 7.2.: Hyperfine splittings of the excited state of the ^{163}Dy and ^{161}Dy fermionic isotopes.

From the assignation, we see that the "163 : 9.5" transition peak is sitting on top of the ^{162}Dy one. In addition there is one non assigned peak with this procedure, which we identify with the ^{160}Dy boson. Similarly to figure 2.2 we can calculate the hyperfine structure for the fermionic isotopes of the excited state shown in figure 7.2.
This is the first time this was measured on the ^{163}Dy and the ^{161}Dy fermionic isotopes for the 684 nm transition.

Experimental Assignment of the Hyperfine Transitions

It is possible to get a proof of the assignment experimentally. To do so we use a beam at 421 nm as pump beam and a beam at 684 nm to probe the transition. Here, we do not frequency scan the pump beam but fix it to a specific transition. As the assignment of the 421 nm spectrum is well known, we know which transition is pumped and with this we also know which transition can be probed. Still, one has to be careful that, as the two laser beams are acting on different excited states, this procedure is not a real doppler-free measurement. If we frequency lock the blue laser to a transition, we not only pump this transition but also the full doppler-broadened line around this transition.
An example plot on the ^{163}Dy fermion is shown in figure 7.3. Here, the frequency of the blue pump laser is set to the $163 : 10.5 \rightarrow 11.5$ transition. The red probe leaser is scanned in frequency over the spectrum.
We first observe that the 163 : 10.5 peak appears at the same relative frequency as the one of the reference spectrum. This implies that we are acting on the same velocity class compared to the reference spectrum. Additionally, as already mentioned, we are not only probing one velocity class but also the Doppler-broadening around the blue $163 : 10.5 \rightarrow 11.5$ transition. This includes the following transitions: $163 : 9.5 \rightarrow 10.5$, $163 : 8.5 \rightarrow 9.5$ and the the transition of the 164 boson. The peaks contributing to the mentioned transitions are assigned in the figure. However, their relative frequencies do

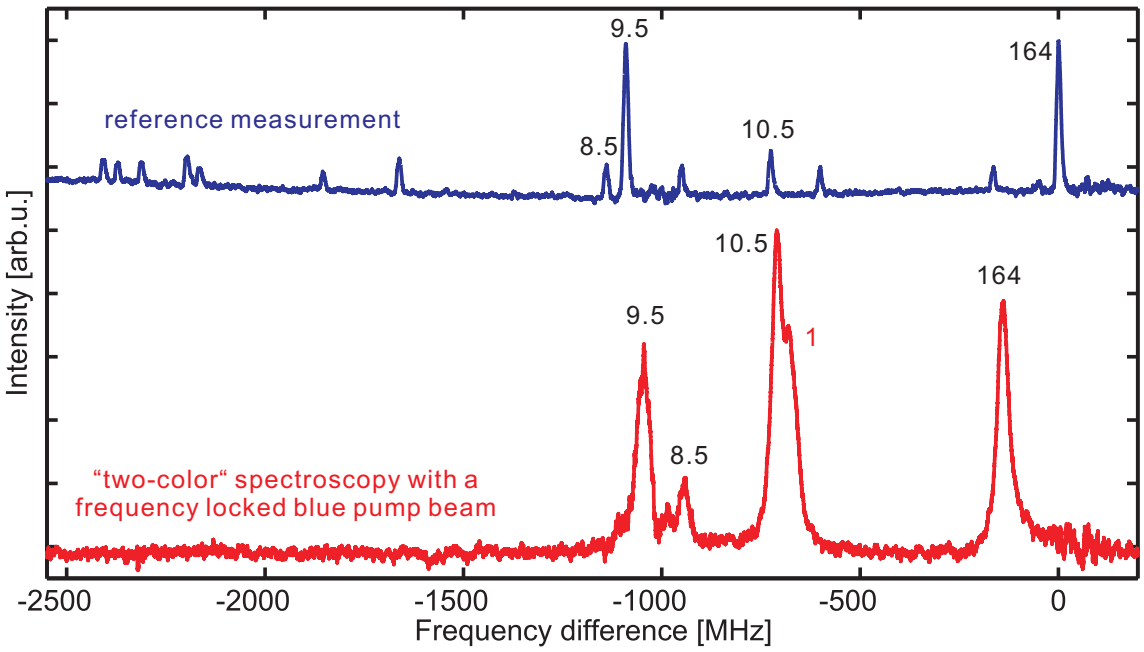

Figure 7.3.: Example for the experimental determination of the hyperfine splittings. The upper blue graph shows the reference signal, which is the same spectrum as in figure 7.1, where we pump and probe with the 684 nm laser beam. The lower red graph shows the measured signal, when we pump the $163 : 10.5 \rightarrow 11.5$ transition with 421 nm laser beam and probe with the 684 nm laser beam.

not match with the ones of the reference spectrum as they are acting on different velocity classes. Furthermore, at the transition peak for the $163 : 10.5$ transition we observe a shoulder (marked as 1). From the calculations we can assign this peak as the following: the blue pump beam is acting on the $163 : 9.5 \rightarrow 8.5$ transition while the red probe beam acts on the $163 : 9.5 \rightarrow 10.5$ transition.

Isotope Shifts

The measured isotope shifts for the 684 nm transition are shown in the table 7.3.

	684 nm shifts [MHz]	457 nm shifts [MHz]
^{164}Dy	0	0
^{163}Dy	-821.7(1)	660(3)
^{162}Dy	-1091.1(1)	971(2)
^{161}Dy	-2100.6(1)	1744(3)
^{160}Dy	-2308.7(1)	2020(3)

Table 7.3.: Isotope shifts, related to the ^{164}Dy boson, for the 684 nm transition and the 457 nm transition used as reference [44].

To analyze the electronic nature of the transition, a King plot [45] is performed. In a King plot one usually plots the obtained isotope shifts for a transition, normalized to the difference in atomic number, as a function of the normalized isotope shifts for a well known reference transition. This reference should have a purely electronic configuration, which is why the 457 nm transition is used [44]. The King plot for the 684 nm transition is shown in figure 7.4. The different isotope shifts are coming from different masses and

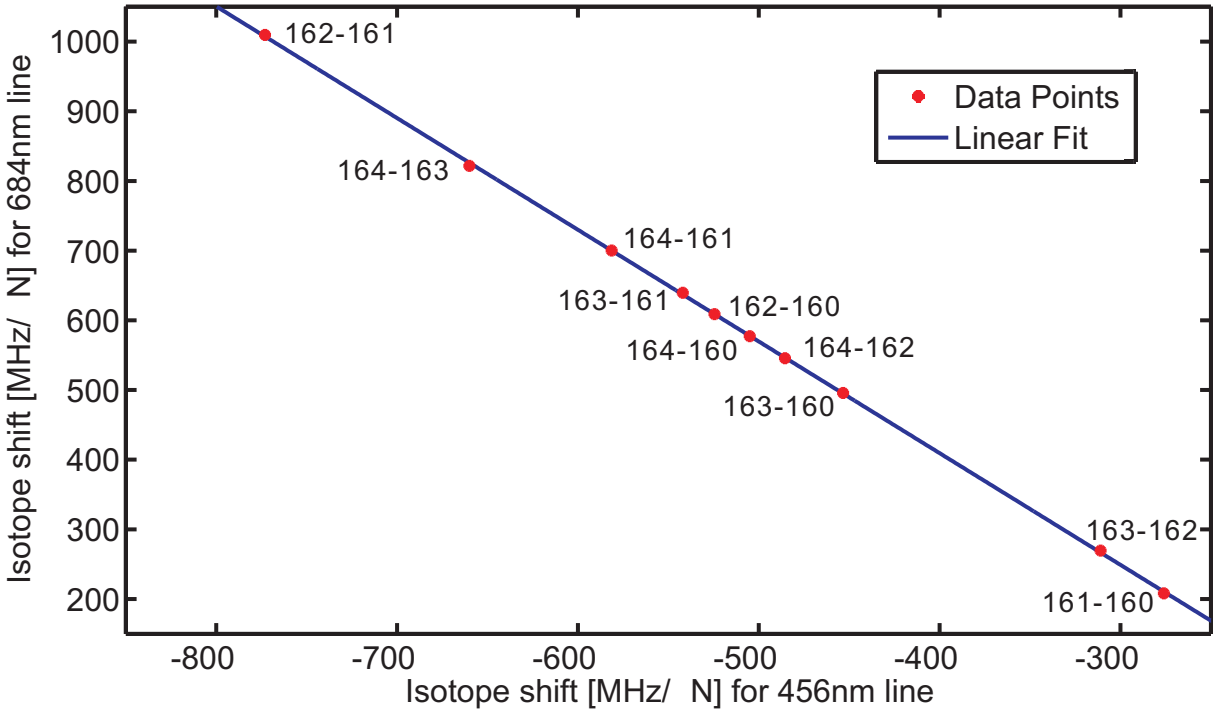

Figure 7.4.: King plot giving the normalized isotope shifts for the 684 nm transition as function of the ones for the 457 nm transition. A linear fit was plotted to the data. The error bars on the isotope shifts are smaller than the size of the points.

volumes of the nuclei of the isotopes. Calculations show that the shift is caused by the field shift (FS), the normal mass shift (NMS) and the specific mass shift (SMS): The FS comes from the change in nuclear charge distribution; the NMS is due to the reduced mass of the electron and the nucleus; the SMS is caused by the influence of the motion of the electron on the recoil energy of the nucleus. The equation describing these effects is given by [22]

$$\delta\nu_{\mathrm{i}} = \frac{E_{\mathrm{i}}}{E_{\mathrm{j}}}\delta\nu_{\mathrm{j}} + \delta\nu_{\mathrm{iNMS}} + \delta\nu_{\mathrm{iSMS}} - \frac{E_{\mathrm{i}}}{E_{\mathrm{j}}}\left(\delta\nu_{\mathrm{jNMS}} + \delta\nu_{\mathrm{jSMS}}\right) , \tag{7.3}$$

with the isotope shifts of the transitions i and j $\delta\nu_{\mathrm{i,j}}$, the NMS $\delta\nu_{\mathrm{i,jNMS}}$, the SMS $\delta\nu_{\mathrm{i,jSMS}}$ and the electronic field shift parameter $E_{\mathrm{i,j}}$. The NMS can be analytically calculated by

$$\delta\nu_{\mathrm{i,jNMS}} = \frac{\nu_{i,j}}{1836.15}\frac{A' - A}{AA'} , \tag{7.4}$$

with $(A,\, A')$ the mass number of the considered isotopes and the transition frequencies $\nu_{\mathrm{i,j}}$. Here, the index i describes the 684 nm transition and the index j the reference transition at 457 nm. We can bring equation (7.3) in a form allowing to directly fit the King plot:

$$\frac{\delta\nu_{\mathrm{i}}}{A'-A} = \frac{E_{\mathrm{i}}}{E_{\mathrm{j}}}\frac{\delta\nu_{\mathrm{j}}}{A'-A} + \left[\frac{\delta\nu_{\mathrm{iNMS}}+\delta\nu_{\mathrm{iSMS}}}{A'-A} - \frac{E_{\mathrm{i}}}{E_{\mathrm{j}}}\frac{\delta\nu_{\mathrm{jNMS}}+\delta\nu_{\mathrm{jSMS}}}{A'-A}\right]. \tag{7.5}$$

From a linear fit to the King plot, we extract the slope which directly gives the field shift parameter ratio $\frac{E_{684}}{E_{457}} = -1.603 \pm 0.006$ and the intersection $b = -231.918 \pm 3.206\,\mathrm{MHz}$, which allows to calculate the SMS for the 684 nm transition. To do so, we still need to know the NMS for the 684 nm transition and the NMS and SMS for the reference transition. For the two most abundant bosons, the NMS for the 684 nm transition is calculated with equation (7.4) to $\delta\nu^{164-162}_{684\mathrm{NMS}} = 18\,\mathrm{MHz}$. The NMS and the SMS values for the reference transition are taken from [44]: $\delta\nu^{164-162}_{457\mathrm{NMS}} = 27\,\mathrm{MHz}$, $\delta\nu^{164-162}_{457\mathrm{SMS}} = 7\,\mathrm{MHz}$. This finally leads to an SMS for the isotopes ^{164}Dy and ^{162}Dy of

$$\delta\nu^{164-162}_{684\mathrm{SMS}} = 2b - \delta\nu^{164-162}_{684\mathrm{NMS}} + \frac{E_{\mathrm{i}}}{E_{\mathrm{j}}}\left(\delta\nu^{164-162}_{457\mathrm{NMS}} + \delta\nu^{164-162}_{457\mathrm{SMS}}\right) = -536 \pm 12\,\mathrm{MHz}\,.$$

Both, the negative FS parameter ratio and the highly negative SMS indicate the very different nature of the two transitions: For the measured 684 nm transition, the binding energies of the involved electron to the nucleus and the electron correlations itself are strong and indicate that this is an inner shell transition: in this case $4f^{10}6s^2 \rightarrow 4f^{9}5d6s^2$. On the contrary, the 457 nm transition is an outer shell transition, $4f^{10}6s^2 \rightarrow 4f^{10}6s6p$, with a small SMS, which is why it is usually chosen as reference transition for King plots. The SMS for this transition was already observed in ref. [22] to be $\delta\nu^{164-162} = -575(18)\,\mathrm{MHz}$. In their case they only considered the bosonic isotopes and took a different reference transition for their King plot. Nevertheless, the SMS for such a $4f^{10}6s^2 \rightarrow 4f^{9}5d6s^2$ transition has been measured for the same two isotopes in ref. [44] for different transitions to be $\delta\nu^{164-162} = -529(14)\,\mathrm{MHz}$. We find our value within those errorbars.

7.3. Fluorescence Spectroscopy

As we could not measure the linewidth of the transition with the saturated absorption spectroscopy, we used fluorescence spectroscopy (see 4.1.2): We set the frequency on resonance to the transition and look at the decay of the fluorescence light when chopping the laser using an AOM. The result is shown in figure 7.5. The strength of this signal was about $10\,\mu\mathrm{V}$ on the photodiode, which is why we had to average 10000 times and take a mean average of 100 points to see the signal. From an exponential fit to the fluorescence signal we extract the decay time of $\tau = 1.666 \pm 0.036\,\mu\mathrm{s}$. With this we can calculate the linewidth of the transition to $\gamma = 95.53 \pm 2.11\,\mathrm{kHz}$. As already mentioned, for this kind of measurement, we need to make sure that the photodiode and the AOM used to chop the light are fast enough. We used a commercial photodiode with a 10dB amplification. This

photodiode has a bandwidth of $BW = 12.5\,\mathrm{MHz}$, so a risetime of $t = 80\,\mathrm{ns}$. The risetime of the AOM is on the same order of magnitude. Therefore we should not be limited by the speed of the photodiode and the AOM. To ensure this we tested two different photodiodes and measure the decay time with them (see table 7.4):

photodiode	risetime [ns]	measured decaytime [μs]	linewidth [kHz]
PDA10	6.66	1.949(38)	81.66(162)
PDA36 (0dB)	58.82	1.482(84)	107.39(645)
PDA36 (10dB)	80	1.666(36)	95.53(211)

Table 7.4.: Excited state lifetime measured with different photodiodes and the corresponding calculated linewidth. The error on the lifetime is coming from the fit. The dB values in brackets give the amplification of the photodiode Thorlabs PDA36.

From the different measurements, we determine the mean value for the linewidth and find the natural linewidth of the transition to be

$$\gamma_{684} = 95 \pm 13\,\mathrm{kHz}\,.$$

This is the first measurement on the lifetime of the excited state from the 684 nm transition.

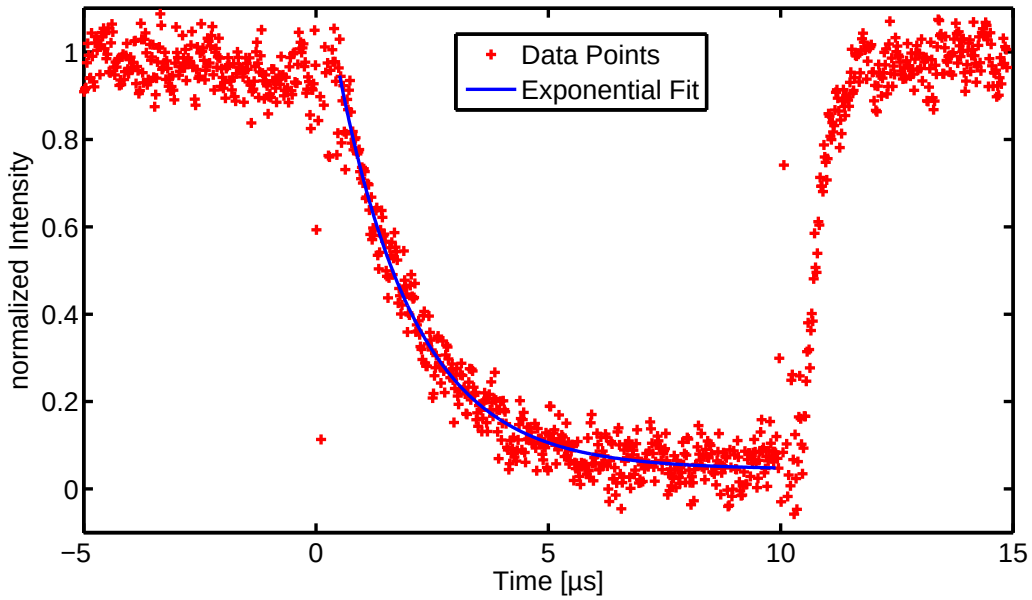

Figure 7.5.: Decay of the fluorescence light. The data points (red crosses) are averaged over 10000 single shots and a mean average of 100 points was applied afterwards to get the signal, which is shown. The blue line corresponds to an exponential fit to the data.

7.4. Polarization Spectroscopy

As a last measurement we change the setup to perform the polarization spectroscopy as we want to frequency-lock the laser to this transition. We see that the signal is not symmetric around zero if the intensity is too strong compared to the saturation intensity. With a pump power $P_{\text{pump}} = 150\,\mu\text{W}$ and a probe power $P_{\text{probe}} = 60\,\mu\text{W}$ we were still able to measure a signal, shown in figure 7.6, and find it quite symmetric around zero. With this single shot picture, we get a frequency RMS of $\nu_{\text{RMS}} = 129.4\,\text{kHz}$, which is bigger than the natural linewidth of the transition and therefore the polarization spectroscopy signal is not yet good enough to frequency-lock the laser to the transition. Here the ν_{RMS} is calculated the same way as in subsection 6.3.
To be able to lock the laser to this transition one has to decrease the ν_{RMS}. To do so, one can either increase the signal to noise ratio or use a lower laser intensity leading to a smaller linewidth, which was currently measured to be $\gamma = 1.7 \pm 0.2\,\text{MHz}$.

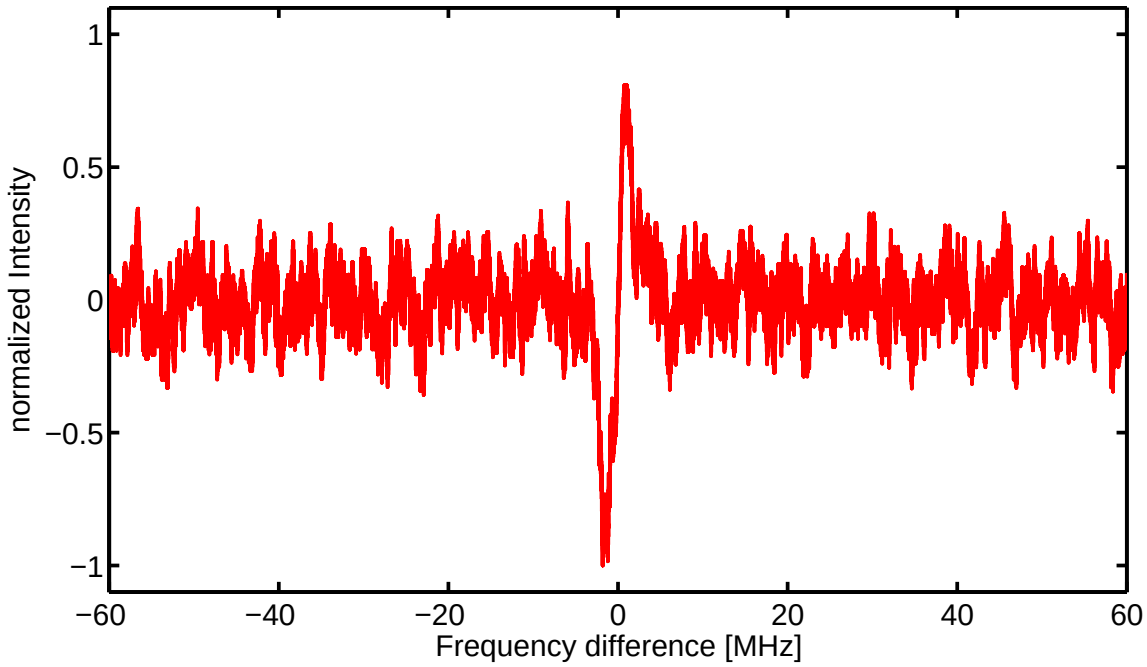

Figure 7.6.: Probe transmission signal obtained with polarization spectroscopy. From the intensity RMS we can calculate the frequency RMS to see if this signal is sufficient for a frequency lock to the transition.

8. Conclusion and Outlook

Conclusion

In this thesis we presented spectroscopic results on two important transitions for the study of dysprosium, which in our context means towards a quantum degenerate atomic gas: the 421 nm cooling transition and the 684 nm optical pumping transition.

Investigating the 421 nm transition, we measured the natural linewidth to be $\gamma_0 = 30.87 \pm 0.27$ MHz. This value matches the one measured in ref. [20] when considering additional errors coming from the frequency scan of our laser. With the theory described in section 3.1, we could explain all visible features observed in the measured spectrum. We frequency-locked the laser to the polarization spectroscopy signal of the ^{164}Dy isotope with an accuracy on the frequency of $\nu_{\mathrm{RMS}} = 0.61$ MHz. This has allowed us to sucessfully slow atoms in a Zeeman slower and trap them in a magneto-optical trap (MOT).

Furthermore, we measured the natural linewidth of the 684 nm transition to be $\gamma_0 = 95 \pm 13$ kHz. Additionally we were able to assign the hyperfine transitions and found the hyperfine constants of the excited state to be

hyperfine constants	A_{e} [MHz]	B_{e} [MHz]
^{161}Dy	-108.95	2249.66
^{163}Dy	152.55	2352.61

Within this measurement we observed the isotope shifts for the five highest natural abundant isotopes to be

isotope shifts	684 nm shifts [MHz]
^{164}Dy	0
^{163}Dy	-821.7(1)
^{162}Dy	-1091.1(1)
^{161}Dy	-2100.6(1)
^{160}Dy	-2308.7(1)

As a proof to our assignation, we performed a "two-color" spectroscopy measurement to the spectrum. To the best of our knowledge, this was the first time that the natural linewidth was measured and the isotope assignation of this transition was performed. With the 457 nm transition as a reference, we calculated the specific mass shift between the ^{164}Dy and the ^{162}Dy isotopes to be $\delta\nu_{684\mathrm{SMS}}^{164-162} = -536 \pm 12$ MHz, which differs from the

results obtained in ref. [22] but is in a good agreement with the measurements done in ref. [44]. Finally, we were able to measure a polarization spectrum of the ^{164}Dy bosonic transition.

Outlook

With the stable polarization-spectroscopy lock of the 421 nm light, we have already been able to slow the atoms in a Zeeman-slower and trap them in a MOT. The next step will be to create a quantum degenerate atomic gas to be able to study strong dipolar effects in dysprosium.

Further investigations on the 684 nm polarization spectroscopy have to be done to frequency-lock the laser to this transition. As the 684 nm transition is not a closed transition, the use of a repumping laser at a wavelength of 953 nm might be important. So far, this transition is completely unknown, which makes it an interesting candidate for future spectroscopic analysis. Additionally, as already mentioned in the introduction, dysprosium is a very good candidate for further investigations in the search for the variation of the fine-structure constant. Dysprosium is already used in this field of research [18] using the following excitation scheme: the first excitation step from the groundstate **G**

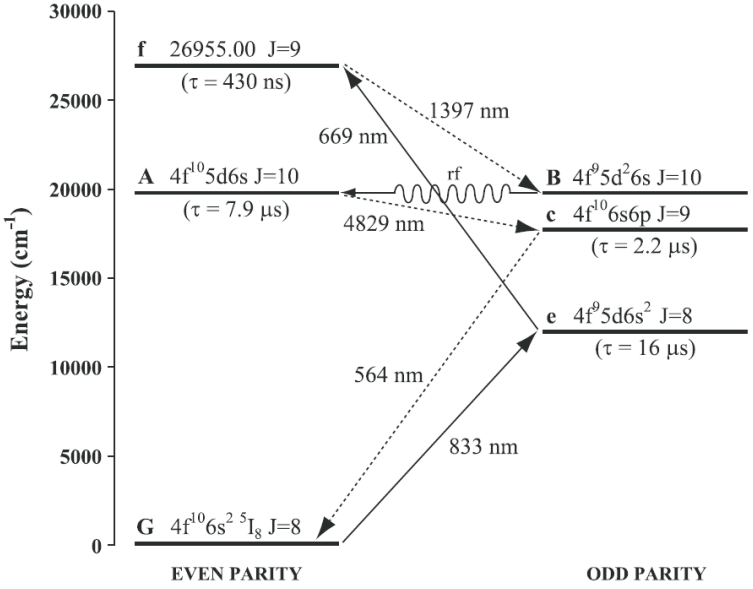

Figure 8.1.: Excitation scheme for the investigation of a variation of the fine-structure constant from ref. [18].

to the excited state **e** is a $J \rightarrow J$ transition. This first excitation could be replaced with the 684 nm transition, which was characterized within this thesis. With this, the second excitation to the excited state **f** would need a wavelength of around $\lambda \approx 811$ nm. This is likely to become a future line of investigation.

9. Zusammenfassung der Masterarbeit

Inhalt dieser Arbeit ist die spektroskopische Untersuchung zweier optischer Übergange des Elements Dysprosium. Es handelt sich dabei um einen starken Kühlübergang bei einer Wellenlänge von 421 nm und einem Übergang zum optischen Pumpen magnetischer Unterzustände bei einer Wellenlänge von 684 nm. Der Übergang bei 421 nm wurde bereits charakterisiert [20, 23], während der Übergang bei 684 nm bisher nur teilweise bekannt ist [22].

Während den Messungen zum 421 nm Übergang konnten wir die bereits veröffentlichten Ergebnisse innerhalb unserer Fehlerbalken bestätigen. So wurde die natürliche Linienbreite des Übergangs durch eine Leistungsserie in Sättigungsspektroskopie bestimmt zu $\gamma_0 = 30.87 \pm 0.27\,\mathrm{MHz}$. Zusätzlich konnten wir mit Hilfe der in Kapitel 3.1 vorgestellten Theorie zur Hyperfeinstruktur alle sichtbaren Strukturen im gemessenen Spektrum erklären und damit alle Resonanzen den zugehörigen Übergangen, sowohl für bosonische als auch fermionische Isotope, zuweisen. Ziel der Spektroskopie an diesem Übergang war es die Laserfrequenz auf einen der Isotopenübergänge zu stabiliseren. Hierzu nutzten wir die Dopplerfreie Polarisationsspektroskopie und untersuchten die Signalform in Abhängigkeit eines angelegten Magnetfeldes und der Temperatur. Im speziellen Fall unseres experimentellen Aufbaus stellte sich heraus, dass die Amplitude des gemessenen Signals bereits ab einem Magnetfeld von $B = 2\,\mathrm{G}$ sättigt. Die Temperaturabhängigkeit zeigte den erwarteten Verlauf nach der Antoine-Gleichung [42]. Zur Stablisierung des Lasers ist es wichtig, dass das Signal-Rausch-Verhältnis groß genug ist, dass eine dauerhafte Frequenzstabiliserung auf der Resonanz des Übergangs gewährleistet wird. Dazu wurde der Effektivwert (*engl.* root mean square, RMS) der Intensität gemessen und mit Hilfe der Frequenzflanke des Fehlersignals in einen Frequenz-Effektivwert umgerechnet zu $f_{\mathrm{RMS}} = 0.61\,\mathrm{MHz}$. Verglichen mit der natürlichen Linienbreite des Übergangs von 32.2 MHz [20] können wir damit sicherstellen, dass das Signal zur Frequenzstabilisierung des Lasers geeignet ist und konnten bereits, bei frequenzstabilisertem Laser, Atome mit einem Zeeman-Abbremser abbremsen und anschliessend in einer magneto-optischen Falle (*engl.* magneto-optical trap (MOT)) einfangen.

Der Übergang bei 684 nm wurde ebenfalls innerhalb dieser Arbeit vermessen. Die natürliche Linienbreite wurde über den exponentiellen Zerfall der Fluoreszenz bestimmt zu

$$\gamma_0 = 95 \pm 13\,\mathrm{kHz}\,.$$

Mit der Sättigungsspektroskopie konnten die fünf Isotope mit der höchsten natürlichen Häufigkeit vermessen und zugewiesen werden. Die Zuweisung der fermionischen Hyperfeinstruktur wurde erneut mit der Theorie aus Kapitel 3.1 berechnet. Dadurch wurden die (A,B) Konstanten der Hyperfeinstruktur bestimmt zu:

Konstanten der Hyperfeinstruktur	A_e [MHz]	B_e [MHz]
^{161}Dy	-108.95	2249.66
^{163}Dy	152.55	2352.61

Aus dem gemessenen Spektrum (siehe Abbildung 7.1) und der Hyperfeintheorie wurde anschliessend die Isotopieverschiebung bestimmt zu:

Isotopieverschiebung	684 nm Verschiebung [MHz]
^{164}Dy	0
^{163}Dy	-821.7(1)
^{162}Dy	-1091.1(1)
^{161}Dy	-2100.6(1)
^{160}Dy	-2308.7(1)

Die Zuweisung wurde zusätzlich durch eine simultane Messung mit dem bekannten 421 nm Übergang und dem 684 nm Übergang bestätigt. Nach unserer Kenntnis haben wir das erste Mal sowohl die Linienbreite des Übergangs gemessen, als auch die Hyperfeinzuweisung berechnet. Mit Hilfe eines Referenzübergangs bei 457 nm [44] wurde eine King-Abbildung des 684 nm Übergangs durchgeführt. Aus diesem wurde die spezifische Massenverschiebung (*engl.* specific mass shift, SMS) zwischen den bosonischen Isotopen ^{164}Dy und ^{162}Dy bestimmt zu $\delta\nu_{684\mathrm{SMS}}^{164-162} = -536 \pm 12\,\mathrm{MHz}$. Diese Messung wurde bereits in Referenz [22] durchgeführt. Die Werte unterscheiden sich um weniger als 10%, allerdings wurde bei unserer Messung ein anderer Referenzübergang benutzt. In Referenz [44] hingegen wurde die spezifische Massenverschiebung systematisch für verschiedene Elektronenübergange untersucht und wir finden unseren Wert in guter Übereinstimmung mit den dort gemessenen Ergebnissen. Schlussendlich wurde ein Polarisationsspektrum des ^{164}Dy Isotopes vermessen. Aus der Messung folgern wir, dass das Signal-Rausch-Verhältnis weiter verbessert werden muss, um den Laser auf diesen Übergang zu stabilisieren.

A. Appendix

A.1. Spectroscopy with a Hollow Cathode Lamp

As described in chapter 5 we searched for different dysprosium atom sources. The first approach, based on an atomic beam, was presented in section 5.2. The second approach for this is the use of a hollow cathode lamp. This technique was successfully used for chromium as shown in ref. [46, 47].

A.1.1. Setup

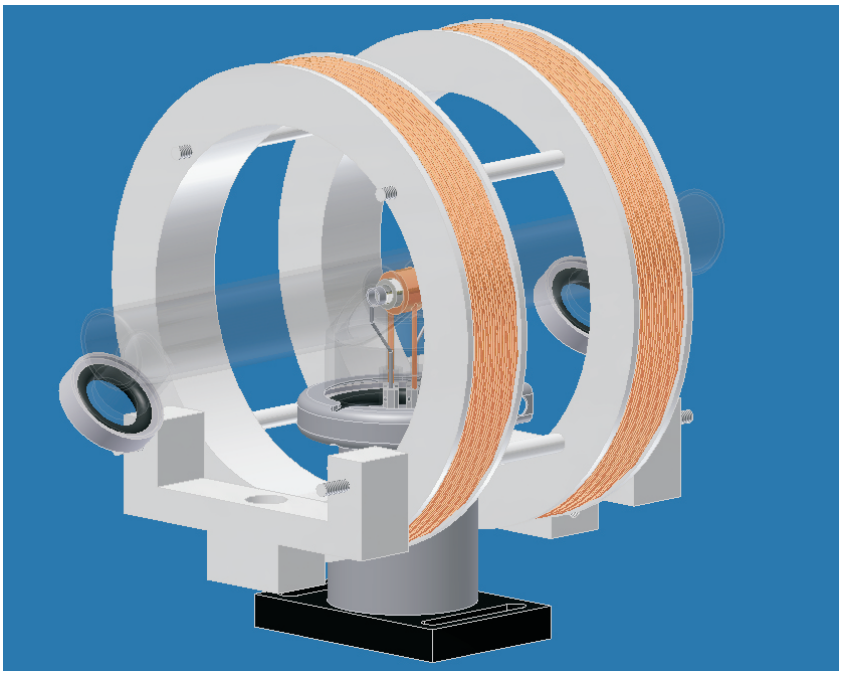

Figure A.1.: Technical drawing of the hollow cathode lamp.

The hollow cathode lamp is designed similarly to the one used in chromium and can be seen in figure A.1. The cathode is composed of a 14 mm-long dysprosium cylinder[1], with an inner diameter of 6 mm and an outer diameter of 9 mm. The dysprosium cylinder is pressed inside a copper cylinder. The copper cylinder prevents electrical contacts to the

[1]Made by the company "Hauner, metallische Werkstoffe"

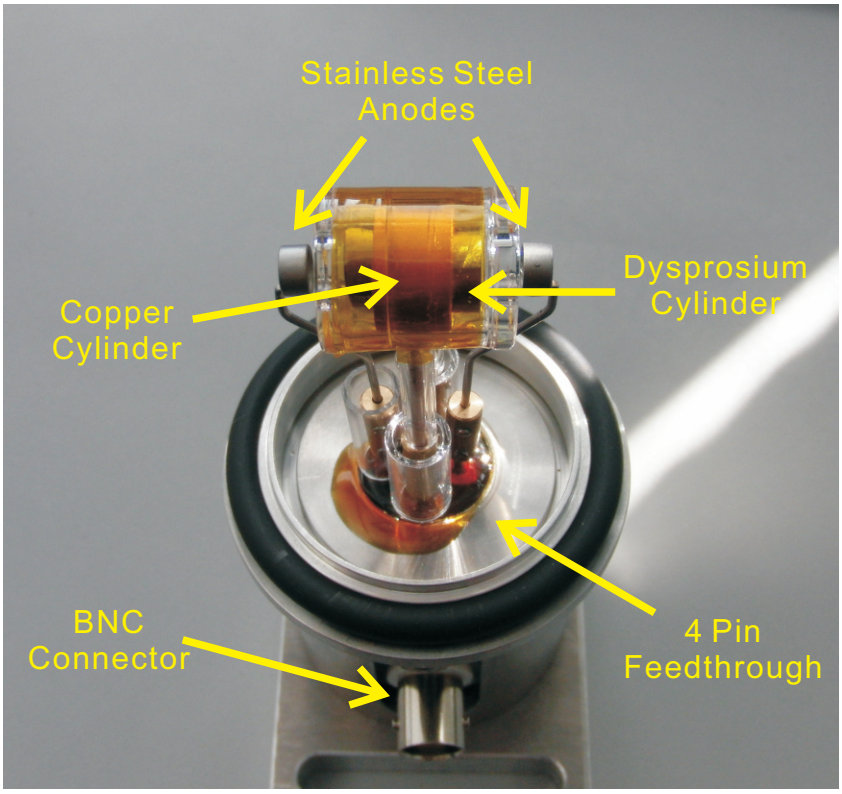

Figure A.2.: Picture of the hollow cathode lamp showing the dysprosium cylinder cathode and the two ring-shaped anodes. The cathode is covered with glass tubes to ensure that there are no electric discharges to the feedthrough or the anodes.

dysprosium cylinder and is stabilized by two rods mounted to two pins of a commercial four-pin electrical feedthrough. Except for the hole of the dysprosium cylinder, the whole cathode is covered with glass tubes to protect the setup from electrical discharges. In addition the lower part of the feedthrough is filled with an electrically insulating glue[2]. Two rings made of stainless steel are used as anodes and are mounted on the two remaining pins of the electrical feedthrough (see figure A.2). The electrical contacts were made such that the cathode has a negative potential and the two anodes are grounded with the power supply such that a BNC connector can be used. As we want to have the setup under low pressure and flooded with a noble gas, it is covered with a huge glass tube, mounted to the electrical feedthrough via a KF40 flange. The glass tube itself has two KF16 flanges mounted to a bellow for the noble gas flooding. An oil- free scroll pump[3] with a needle valve to control the pressure and thereby the gas flow through the cylinder is mounted to one end of the glass tube. We used argon as noble gas with a pressure of $p_{cathode} = 1\,\mathrm{mbar}$ and apply a voltage of $U = -400\,\mathrm{V}$.

[2]EpoTek 353ND
[3]Ulvac DIS-251

A.1.2. Sputter Effect

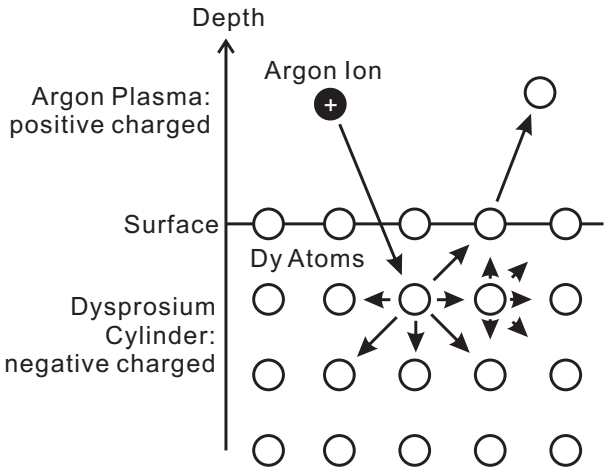

Figure A.3.: Principle of the sputter effect. Positive charged argon ions are accelerated to the negative charged dysprosium cylinder and kick out dysprosium atoms.

The hollow cathode lamp is based on the sputter effect and the principle of this effect is shown in figure A.3. Due to the high voltage applied to the cathode the argon gas flooding through the cylinder is ionized and an argon plasma is burning. The argon ions are accelerated to the dysprosium cylinder and kick out the outer dysprosium atoms. With this we create a dense sample of dysprosium atoms in the middle of the cylinder.

A.1.3. Result

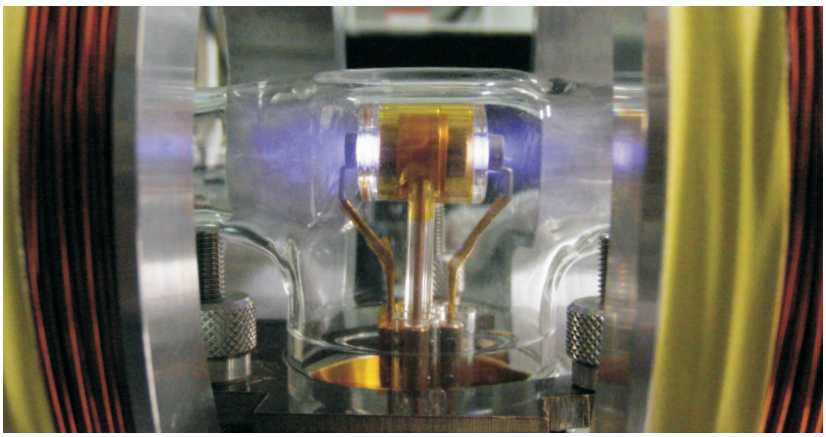

Figure A.4.: Picture of the hollow cathode lamp with the argon plasma inside the cylinder.

After polishing the cylinder and the anodes, we were able to create a stable argon plasma in the cathode as can be seen in figure A.4. But the plasma was stable for only one

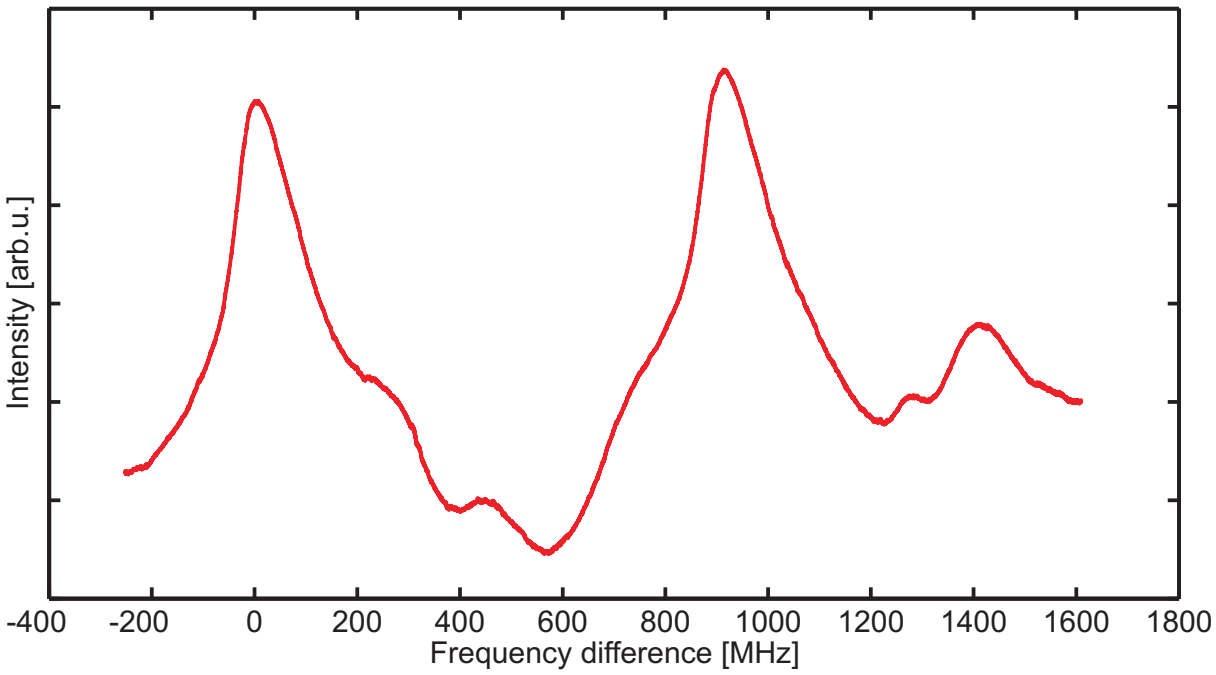

Figure A.5.: Measured spectrum of the 421 nm transition with the hollow cathode lamp using the saturation spectroscopy technique.

day. Nevertheless, during this time we could measure the spectrum shown in figure A.5. We see very broad spectral lines. A Lorentzian fit to the peak at relative frequency zero gives a linewidth of $\gamma = 178 \pm 2\,\mathrm{MHz}$. Because of the pressure broadening, the line is even broader than what was measured in fluorescence spectroscopy (see section 6.1). In addition one can only make a rough guess about the assignement of the peaks.
As already mentioned, the plasma was only stable for one day. There are two possible reasons for this. The first problem occured when the dysprosium cylinder had to be pressed in the copper cylinder. During this process, the dysprosium cylinder was damaged at one point. Another problem might be the use of the copper cylinder. So far, we always used stainless steel cylinders for the electrical contact [46, 47]. We have seen flashovers between the two cylinders, which is only possible if both have a different electric potential. This means that there might be a chemical reaction between the copper and the dysprosium, leading to an insulating layer between both.

A.2. Estimation of the Linewidth for the 684nm Optical Pumping Transition

In this section we want to present an idea how to estimate the linewidth of a transition, using as an example the 684 nm transition. The idea is to compare the relative intensities from the NIST atomic spectra database and with this conclude on the linewidth. The rel-

ative intensity is proportional to the oscillator strength f_{ik} and the transition wavelength, so we can write [48]

$$\frac{I_{\mathrm{rel1}}}{I_{\mathrm{rel2}}} = \frac{f_{\mathrm{ik1}}\lambda_1}{f_{\mathrm{ik2}}\lambda_2}\,. \tag{A.1}$$

The oscillator strength can be described by the emission transition probability A_{ki}, the statistical weight g_{k} and the transition wavelength leading to

$$\frac{I_{\mathrm{rel1}}}{I_{\mathrm{rel2}}} = \frac{A_{\mathrm{ki1}}\lambda_1^3 g_{\mathrm{k1}}}{A_{\mathrm{ki2}}\lambda_2^3 g_{\mathrm{k2}}}\,. \tag{A.2}$$

The linewidth of a transition is defined by $\gamma = \frac{A_{\mathrm{ki1}}}{2\pi}$. If we plug this into equation (A.2) we can write

$$\gamma_2 = \frac{\gamma_1\lambda_1^3 g_{\mathrm{k1}} I_{\mathrm{rel2}}}{\lambda_2^3 g_{\mathrm{k2}} I_{\mathrm{rel1}}}\,. \tag{A.3}$$

With this equation we can now calculate the linewidth of the 684 nm transition depending on a different known transition. During the calculation we assumed that such a reference transition is starting from the groundstate. We show some estimated linewidths in the following table

reference transition	γ_{684} [kHz]
421 nm	94
459 nm	50
626 nm	77
estimation from [26]	350

Table A.1.: Estimation of the linewidth for different reference transitions.

We see that the linewidth calculation is strongly depending on the reference transition and does not lead to the same result, which is why it was estimated to be $\gamma_{684} = 50 - 350\,\mathrm{kHz}$ in the beginning (see chapter 2).

Bibliography

[1] M. Anderson, J. Ensher, M. Matthews, C. Wieman and E. Cornell, *Observation of Bose-Einstein condensation in a dilute atomic vapor*, Science, **269**, 198–201 (1995).

[2] K. Davis, M. Mewes, M. Andrews, N. van Druten, D. S. Durfee, D. Kurn and W. Ketterle, *Bose-Einstein Condensation in a Gas of Sodium Adoms*, Phys. Rev. Lett., **75**, 3969–3973 (1995).

[3] C. Bradley, C. Sackett, J. Tollett and R. Hulet, *Evidence of Bose-Einstein Condensation in an Atomic Gas with Attractive Interactions*, Phys. Rev. Lett., **75**, 1687–1690 (1995).

[4] C. Chin, R. Grimm, P. Julienne and E. Tiesinga, *Feshbach resonances in ultracold gases*, Rev. Mod. Phys., **82**, 1225–1286 (2010).

[5] A. Griesmaier, J. Werner, S. Hensler, J. Stuhler and T. Pfau, *Bose-Einstein Condensation of Chromium*, Phys. Rev. Lett., **94**, 160401 (2005).

[6] M. Baranov, *Theoretical progress in many-body physics with ultracold dipolar gases*, Physics Reports, **464**, 71–111 (2008).

[7] T. Lahaye, C. Menotti, L. Santos, M. Lewenstein and T. Pfau, *The physics of dipolar bosonic quantum gases*, Rep. Prog. Phys., **72**, 126401 (2009).

[8] T. Lahaye, T. Koch, B. Fröhlich, M. Fattori, J. Metz, A. Griesmaier, S. Giovanazzi and T. Pfau, *Strong dipolar effects in a quantum ferrofluid*, Nature, **448**, 672–675 (2007).

[9] T. Koch, T. Lahaye, J. Metz, B. Fröhlich, A. Griesmaier and T. Pfau, *Stabilizing a purely dipolar quantum gas against collapse*, Nature Physics, **4**, 218–222 (2008).

[10] S. Müller, J. Billy, E. A. L. Henn, H. Kadau, A. Griesmaier, M. Jona-Lasinio, L. Santos and T. Pfau, *Stability of a dipolar Bose-Einstein condensate in a one-dimensional lattice*, Phys. Rev. A, **84**, 053601 (2011).

[11] E. Donley, N. Claussen, S. Cornish, J. Roberts and E. C. C. Wieman, *Dynamics of collapsing and exploding Bose-Einstein condensates*, Nature, **412**, 295–299 (2001).

[12] T. Lahaye, J. Metz, B. Fröhlich, T. Koch, M. Meister, A. Griesmaier, T. Pfau, H. Saito, Y. Kawaguchi and M. Ueda, *d-Wave Collapse and Explosion of a Dipolar Bose-Einstein Condensate*, Phys. Rev. Lett., **101**, 080401 (2008).

[13] S. Hensler, J. Werner, A. Griesmaier, P. Schmidt, A. Görlitz, T. Pfau, S. Giovanazzi and K. Rzazewski, *Dipolar Relaxation in an ultra-cold Gas of magnetically trapped chromium atoms*, Appl. Phys. B, **77**, 765 (2003).

[14] M. Fattori, T. Koch, S. Goetz, A. Griesmaier, S. Hensler, J. Stuhler and T. Pfau, *Demagnetization cooling of a gas*, Nature Physics, **2**, 765 (2006).

[15] K. Aikawa, A. Frisch, M. Mark, S. Baier, A. Rietzler, R. Grimm and F. Ferlaino, *Bose-Einstein Condensation of Erbium*, Phys. Rev. Lett., **108**, 210401 (2012).

[16] S. H. Y. Mingwu Lu, Nathaniel Q. Burdick and B. L. Lev, *Strongly Dipolar Bose-Einstein Condensate of Dysprosium*, Phys Rev Lett, **107** (2011).

[17] M. Lu, N. Burdick and B. Lev, *Quantum Degenerate Dipolar Fermi Gas*, Phys. Rev. Lett., **108**, 215301 (2012).

[18] A. Cingöz, N. Leefer, S. Ferrell, A. Lapierre, A. Nguyen, V. Yashchuk, D. Budker, S. Lamoreaux and J. Torgerson, *A laboratory search for variation of the fine-structure constant using atomic dysprosium*, Eur. Phys. J. Special Topics, **163**, 71–88 (2008).

[19] J. Uzan, *The fundamental constants and their variation: observational and theoretical status*, Rev. Mod. Phys., **75**, 403–455 (2003).

[20] S. H. Y. Mingwu Lu and B. L. Lev, *Spectroscopy of a narrow - line laser - cooling transition in atomic dysprosium*, Phys. Rev. A, **83** (2011).

[21] W. Happer, *Optical Pumping*, Rev. Mod. Phys., **44**, 169–249 (1972).

[22] W. Jin, T. Wakui, T. Endo, H. Uematsu, T. Minowa and H. Katsarugawa, *A study of the spectrum of natural dysprosium with the laser-atomic-beam technique. I. Isotope shifts*, Journal of the Physical Society of Japan, **70**, 2316–2320 (2001).

[23] N. Leefer, A. Cingöz and D. Budker, *Measurement of hyperfine structure and isotope shifts in the Dy 421-nm transition*, Optical Letters, **34**, 2548 (2009).

[24] *CRC Handbook of Chemistry and Physics*, CRC Press, New York (2010).

[25] *http://www.webelements.com/dysprosium/isotopes.html*.

[26] S. H. Youn, *PHD Thesis: Bose - Fermi Mixtures of Ultracold Gases of Dysprosium* (2011).

[27] R. W.C. Martin and L.Hagan, *Atomic Energy Levels - The Rare-Earth Elements*, NSRDS-NBS, **60** (1978).

[28] H.Haken and H. Wolf, *The Physics of Atoms and Quanta*, Springer Verlag (2005).

[29] G. Woodgate, *Elementary Atomic Structure*, Oxford University Press (1983).

[30] W. Demtröder, *Laser Spectroscopy Volume 1, Basic Principles*, Springer Verlag (2008).

[31] H. J. Metcalf and P. van der Straten, *Laser Cooling and Trapping*, Springer Verlag (1999).

[32] W. Demtröder, *Laser Spectroscopy Volume 2, Experimental Techniques*, Springer Verlag (2008).

[33] C. P. Pearman, C. S. Adams, S. G. Cox, P. F. Griffin, D. A. Smith and I. G. Hughes, *Polarization spectroscopy of a closed atomic transition: applications to laser frequency locking*, Journal of Physics B: Atomic, Molecular and Optical Physics, **35**, 5141 (2002).

[34] J. D. Jackson, *Klassische Elektrodynamik*, Gruyter Verlag (2006).

[35] J. Werner, *Diplomarbeit: Kontinuierliches Laden einer Magnetfalle mit lasergekühlten Chromatomen* (2000).

[36] *Operator's Manual Verdi V-18, Diode-Pumped Lasers.*

[37] *Operator's Manual MBR Series Lasers, Single Frequency Ti:Sapphire.*

[38] M. Schmitt, *Bachelorarbeit: Laserstabilisierung mit einem hochstabilen Transferresonator* (2010).

[39] *DL100/pro design, Grating Stabilized Diode Laser Head, Manual.*

[40] B. E. A. Saleh and M. C. Teich, *Fundamentals of Photonics*, John Wiley and Sons (2007).

[41] J. W. Childs, *Hyperfine Structure of* $^5I_{8,7}$ *Atomic States of* $Dy^{161,163}$ *and the Ground-State Nuclear Moments*, Phys. Rev. A, **2**, 1692–1701 (1970).

[42] D. Lüdecke and C. Lüdecke, *Thermodynamik: Physikalisch-chemische Grundlagen der thermischen Verfahrenstechnik*, Springer Verlag (2000).

[43] D. Clark, M. Cage and G.W.Greenlees, *The hyperfine structure and hyperfine anomaly of* ^{161}Dy *and* ^{163}Dy, Physics Letters A, **62**, 439–442 (1977).

[44] G. J. Zaal, W. Hogervorst, E. R. Eliel, K. A. H. van Leeuwen and J. Blok, *A study of the spectrum of natural dysprosium with the laser-atomic-beam technique. I. Isotope shifts*, Journal of Physics B: Atomic and Molecular Physics, **13**, 2185 (1980).

[45] D. Budker, D. Kimball and D. DeMille, *Atomic Physics. An Exploration through Problems and Solutions*, Oxford University Press (2008).

[46] P. A. Rehme, *Diplomarbeit: Laden eines Wellenleiters mit lasergekühlten Chromatomen* (2006).

[47] P. Christian, *Diplomarbeit: Stabilisierung eines Lasersystems zur Laserkühlung von Chromatomen* (2009).

[48] W. Martin and W. Wiese, *Atomic Spectroscopy: A Compendium of Basic Ideas, Notation, Data and Formulas*, National Institute of Standards and Technology (2009).

Danksagung

Hiermit möchte ich meinen Dank an folgende Personen ausrichten, die mich während meiner Masterarbeit tatkräftig unterstützt haben, sei es für die Arbeit selbst oder in ausser-physikalischen Belangen:

- Zu aller erst möchte ich **Prof. Dr. Tilman Pfau** danken, für die Ermöglichung dieser Masterarbeit.
- Als nächstes bedanke ich mich bei **Prof. Dr. Jörg Wrachtrup**, dass er die Funktion des Mitberichters übernommen hat.
- Ich danke dem Ex-Chrom / neuen Düsi-Team bestehend aus unserem Gruppenleiter **Dr. Axel Griesmaier**, meinen Betreuern **Holger Kadau** und **Thomas Maier**, meiner Korrekturleserin **Dr. Juliette Billy** und meinem Korrekturleser **Dr. Emanuel Henn** und dem letzten Chromi **Stefan Müller**.
- Weiter möchte ich dem kompletten **5. Physikalischen Institut** danken für die schöne Zeit, die ich hier erleben durfte.
- Zu guter Letzt bedanke ich mich bei **meiner Familie**, **allen Verwandten** und **allen Freunden**, auf die ich zählen konnte, wenn eine physikalische Pause eingelegt werden musste.